# A dual-mode floor isolation system to achieve vibration isolation and absorption: Experiments and theory

P. Bin<sup>a</sup>, P. S. Harvey Jr.<sup>a,\*</sup>

<sup>a</sup>School of Civil Engineering and Environmental Science, University of Oklahoma, Norman, OK 73019, USA

#### **Abstract**

During the event of an earthquake, motion-sensitive equipment inside a building can be protected from seismic disturbance using a floor isolation system (FIS). Its response is unimpeded when it displaces within the allowable clearance, but when this gap is exceeded impacts are induced between the FIS and the displacement limit. This induced nonlinearity may create a non-negligible dynamic coupling between the primary structure (PS) and the FIS, which can possibly be tuned to reduce the PS responses during strong earthquakes. Moreover, the dissipation during impact can be augmented with a shock absorber. This research aims to evaluate the performance of the FIS as a vibration isolator when subjected to low-intensity earthquakes (i.e., before impact occurs) and as a vibration absorber when subjected to high-intensity earthquakes (i.e., after impact occurs). Such a FIS is termed *dual-mode vibration isolator/absorber system* whose quantities of interest concern peak FIS acceleration and peak PS interstory drift when evaluating the isolation performance and the absorption performance, respectively. A lab-scale experimental approach is used to study the FIS performance when attached to the second story of the PS that is subjected to four historic ground motions. Predictions from a mathematical model of the coupled, nonlinear PS-FIS system are compared to the experimental results. The experimental and numerical data shows promising results that suggest the dual performance of the FIS is achieved.

Keywords: vibration isolation, vibration absorption, dual-mode, seismic, impact

#### 1. Introduction

During a seismic event, the intensity of a ground motion (GM) plays an important role in determining the damage state of a structure. For a high intensity disturbance, the GM can cause irreparable damage to structural members, potentially resulting in collapse. In such a scenario, the priority course of action would be to save lives of the building's occupants. Mitigating structural responses during an earthquake can be achieved through a base isolation system [1]. During a small to moderate disturbance, the ground motion of an earthquake may not cause the collapse of a building but could potentially damage expensive and mission-critical equipment inside the building, disrupting business operations. This may include the computers in data centers, displays in a museum, and much more. Therefore, if a structure is expected to be subjected to low-intensity GMs, it can be more economical to focus the engineering design on mitigating the response of such sensitive contents rather than the entire building. Such mitigation can be achieved through a number of methods: (1) isolating the base of an entire building [2, 3, 4, 5], (2) isolating individual objects

Email address: harvey@ou.edu (P. S. Harvey Jr.)

<sup>\*</sup>Corresponding author.

[6, 7, 8, 9, 10, 11], or (3) isolating a raised floor of the structure that objects are placed on [12, 13, 14, 15, 16]. This research is focused on the third method.

Seismic base isolation is a method of elongating the fundamental period of a structure by placing isolation devices at the base of a building to decouple it from the ground [1]. This results in acceleration reduction of structural components during an earthquake. Similar to base isolation system, a floor isolation system (FIS) isolates the objects from the building floor so that the transmission of the floor motion to the objects can be mitigated. The FIS has been a topic of research and discussion for many years now. It has proved to be an effective technique in providing protection to motion-sensitive building contents. Since the FIS decouples the contents from the floor, the transmission of the acceleration from the floor to the contents can be mitigated. There are many types of FISs that have been proposed and tested, including friction pendulum system [12], roll-n-cage isolation system [14], sliding concave foundation system [13], and variable frequency pendulum isolator [17], among others [18]. In past studies, good isolation performance was achieved through proper tuning of the isolation systems' restoring force and damping. However, none of these studies considered the response of the primary structure (PS) in the design of the FIS.

Another vibration mitigation technique is the vibration absorber. As the name implies, this device absorbs (or redistributes) the structure's vibrational energy to help reduce the building (primary system) response. One traditional method to achieve the structure's energy absorption is via the use of tune mass damper (TMD) [19, 20]. In Ref. [21], a number of passive energy dissipation control techniques have been discussed. Among those is a TMD which is a type of dynamic vibration absorber. TMD is a linear approach to passively dissipate energy of PS consisting of a secondary mass that is a fraction (1–5%) of the structures total mass. It has been well established that TMD is effective in reducing wind-induced structural vibration. In term of seismic control, recent research findings have shown that TMD is most effective for a lightly damped structure and when the structure's frequency is close to the GM's frequency [22]. Due to the limitation on suppressing broader frequency range, non-linear dynamic vibration absorbers are preferred because they can overcome the limitation set by linear dynamic vibration absorbers.

Common types of dynamic vibration absorbers are nonlinear energy sink (NES) devices [23, 24]. They have been numerically and experimentally proven to be effective systems in absorbing and dissipating energy of the PS under seismic excitation [25, 26]. Many types of NES devices have been proposed and studied. Nucera et al. [27, 28] introduced the concept of a vibro-impact NES for mitigating seismic response of a structure. Their numerical results showed that vibro-impact NES generates a redistribution of energy from lower to higher mode of the structure. Due to the requirement for large mass for best performance, vibro-impact NES is more effective in transferring momentum when installed at a lower floor. However, NES with smooth nonlinearity are more effective in absorbing seismic energy when attached at a higher floor. This vibro-impact NES concept was later demonstrated experimentally [29]. Wang et al. [30] proposed a new type of NES called "track NES." The performance of the track NES was compared to that of a locked system, linear TMD, and Type I NES (i.e., a single degree of freedom NES with nonlinear stiffness and linear damping attachment [31]). The results showed that the track NES had similar effects on response reduction as Type I NES and could transfer energy from lower mode to the higher mode of the structure. Compared to in-tune TMD, the system was not as effective against seismic excitation, but exhibited robustness against changes in structural stiffness. Wang et al. [32] later proposed and studied the single-sided vibro-impact track NES. This system is designed by adding an impact stopper on one side of the NES mass for the system to provide nonlinearity by smooth nonlinear force-distance relationship and discontinuity in restoring force [33]. The experimental results showed that the single-sided vibro-impact track NES is more effective than the track NES in reducing responses and able to reduce peak PS displacement significantly. Finally, in Ref. [26], a large-scale experiment and numerical simulation for seismic mitigation has been

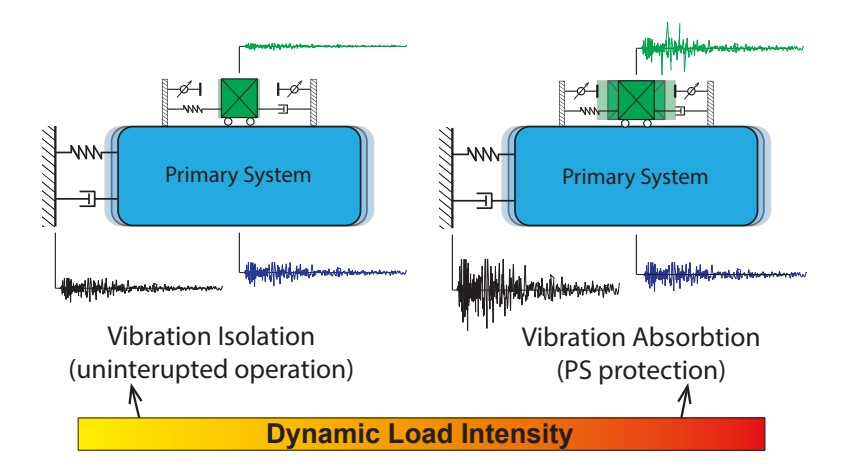


Figure 1: Schematic of a dual-mode vibration isolator/absorber system

studied by combining a system of different types of NES devices on a lab-scaled nine-story structure. Two Type I NESs and one single-sided vibro-impact track NES were installed on the eighth and ninth floor. The building was subjected to base excitation from the shake table that simulates ground motion of three scaled historic earthquakes. The data exhibited the reduction of both peak and root square mean values of the floor displacement, first-story column strain, and base shear. The tests showed that the use of the two NES types combined is more effective in suppressing floor acceleration and displacement compared to the case of using single-sided vibro-impact NESs alone. This result indicated that the NES devices can be combined to provide a very effective means of mitigating structural responses.

Seeing the seismic mitigation potential of both the vibration absorbers and isolation systems, an idea has been recently proposed to combine the two systems into a single *dual-mode vibration isolator/absorber system* [34, 35]. Such a system was designed to passively adapt from an isolation system during small to moderate disturbance to a vibration absorber during larger disturbance amplitude. The latter was to be achieved via impact when the system's displacement exceeded its gap [34]; this concept is illustrated in Fig. 1. Harvey et al. [34] have experimentally shown that such a device proves effective for mitigating the response of a harmonic base excitation, but did not do so for seismic. Reggio and De Angelis [36] have explored a similar concept, but their studies are limited to linear systems, which are incapable of achieving response-based adaptation and performance-based design trade-offs are hazard independent. Therefore, nonlinear behaviors of the combined primary-secondary system under seismic excitation still requires further research, which is the focus of this paper.

This paper describes experimental and theoretical approaches that aim to study the behavior of the dual-mode FIS. In Section 2, the equations of motion for the FIS, PS, and coupled PS-FIS system are formulated, and the performance metrics for evaluating the isolation and absorption performances are defined. The experimental system that details the PS, FIS, and shock absorber are described in Section 3. The experimental protocol that describes the PS-FIS setup, GMs used, and testing procedure are presented in Section 3.5. The experimental and numerical results are discussed in Sections 4 and 5, respectively, followed by conclusions in Section 6.

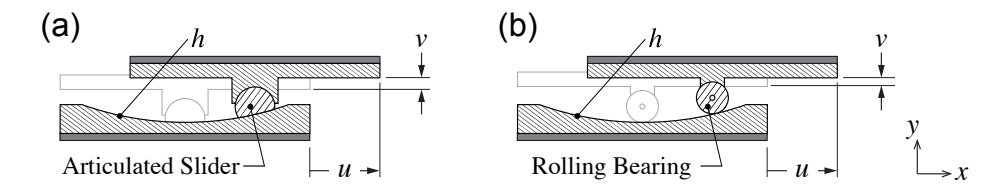


Figure 2: Schematic of (a) friction pendulum bearing and (b) rolling pendulum bearing.

#### 2. Problem Formulation

## 2.1. Floor Isolation System (FIS)

Lagrange's equation is used in this study to derive the equation of motion of the FIS utilizing pendulum bearings like those shown in Fig. 2. The kinetic energy  $\mathcal{T}$  of the FIS comes from the ground motion and the horizontal as well as vertical motion of the FIS itself [37]. The kinetic energy is given by

$$\mathcal{T}(\dot{u}, \dot{v}) = \frac{1}{2}m(\dot{u} + \dot{x}^t)^2 + \frac{1}{2}m(\dot{v} + \dot{y}^t)^2 \tag{1}$$

where u and v denote the horizontal and vertical displacements, respectively, of the FIS relative to the structural floor's total horizontal and vertical displacements,  $x^t$  and  $y^t$ , respectively. The overdot represents the derivative with respect to time, and m denotes the total isolated mass of the FIS.

As the articulated slider or rolling bearing of the FIS moves horizontally, the motion also results in a vertical displacement. The potential energy V of this system is given by

$$\mathcal{V}(v) = mg(v + y^t) \tag{2}$$

where g is the gravitational acceleration. The vertical displacement v is kinematically constrained by the sliding/rolling of the bearings across the concave surface having profile h(u). Hence, the kinematic constraint is written as follows:

$$v = h(u) \tag{3}$$

Thus, the vertical velocity  $\dot{v}$  can be found from the differentiation of Eq. (3) to be

$$\dot{v} = h'(u)\dot{u} \tag{4}$$

Likewise, the vertical acceleration can be obtained by taking the derivative of the velocity to be

$$\ddot{v} = h''(u)\dot{u}^2 + h'(u)\ddot{u} \tag{5}$$

To formulate the equations of motion, the kinematic constraint (Eq. (3)) is handled by the use of a Lagrange multiplier  $\lambda$  as follows:

$$\frac{d}{dt}\frac{\partial \mathcal{L}}{\partial \dot{u}} - \frac{\partial \mathcal{L}}{\partial u} = Q_u + \lambda \frac{\partial \phi}{\partial u} \tag{6a}$$

$$\frac{d}{dt}\frac{\partial \mathcal{L}}{\partial \dot{u}} - \frac{\partial \mathcal{L}}{\partial u} = Q_u + \lambda \frac{\partial \phi}{\partial u}$$

$$\frac{d}{dt}\frac{\partial \mathcal{L}}{\partial \dot{v}} - \frac{\partial \mathcal{L}}{\partial v} = Q_v + \lambda \frac{\partial \phi}{\partial v}$$
(6a)
(6b)

where the Lagrangian  $\mathcal{L} = \mathcal{T} - \mathcal{V}$ ,  $Q_u$  is the sum of forces coming from virtual work due to non-conservative forces (e.g., friction) and the contact force  $f_c$ , and the constraint is given by

$$\phi(u, v) = v - h(u) \equiv 0 \tag{7}$$

Applying this form of Lagrange's equation gives

$$m(\ddot{u} + \ddot{x}^t) = Q_u - \lambda h'(u) \tag{8a}$$

$$m(\ddot{\mathbf{v}} + \ddot{\mathbf{v}}^t) + mg = Q_{\mathbf{v}} + \lambda \tag{8b}$$

From Eq. (8), the force of constraint, which is *normal* to the constraint surface, is given by

$$\mathbf{N} = \lambda \left\{ \frac{-h'(u)}{1} \right\} \tag{9}$$

which has magnitude

$$N = \lambda \sqrt{1 + [h'(u)]^2} \tag{10}$$

Therefore, the normal (constraint) force can be re-written as follows:

$$\mathbf{N} = N \frac{1}{\sqrt{1 + [h'(u)]^2}} \begin{Bmatrix} -h'(u) \\ 1 \end{Bmatrix}$$
 (11)

The forces  $Q_u$  and  $Q_v$  are due to friction  $\mathbf{f}_f$  and the contact force  $\mathbf{f}_c$  of impact. The friction force is perpendicular to  $\mathbf{N}$ , opposing the motion, and is modeled using a Bouc-Wen hysteresis model:

$$\mathbf{f}_f = -\mu N \frac{1}{\sqrt{1 + [h'(u)]^2}} \left\{ \frac{1}{h'(u)} \right\} Z(t)$$
 (12)

The hysteretic displacement Z(t) satisfies

$$\dot{Z}(t) = \dot{s}(t) \{ A - [\beta \operatorname{sgn}(Z(t)\dot{u}(t)) + \gamma] |Z(t)|^n \} / s_{v}$$
(13)

where A,  $\beta$ ,  $\gamma$ , and n are the Bouc-Wen parameters [38],  $\dot{s}(t)$  is the tangential velocity, and  $s_y$  is arc-length displacement over which the full friction force is developed. Using the arc-length relationship:

$$ds^{2} = du^{2} + dv^{2} \Rightarrow \dot{s} = \dot{u}\sqrt{1 + [h'(u)]^{2}}$$
(14)

By substituting Eq. (14) into Eq. (13), the differential equation governing the hysteretic displacement is given by

$$\dot{Z}(t) = \dot{u}(t)\sqrt{1 + [h'(u)]^2} \{ A - [\beta \operatorname{sgn}(Z(t)\dot{u}(t)) + \gamma] |Z(t)|^n \} / s_y$$
(15)

The contact force  $f_c$  from the impact is assumed to be purely in the horizontal (u) direction:

$$\mathbf{f}_c(u, \dot{u}) = \begin{cases} f_c(u, \dot{u}) \\ 0 \end{cases}$$
 (16)

The specific form of the contact force  $f_c$  is discussed in Section 3.3.

From Eqs. (12) and (16), the generalized forces  $Q_u$  and  $Q_v$  are, therefore, given by

$$Q_u = -\mu N \frac{1}{\sqrt{1 + [h'(u)]^2}} Z(t) - f_c(u, \dot{u})$$
(17a)

$$Q_{v} = -\mu N \frac{h'(u)}{\sqrt{1 + [h'(u)]^{2}}} Z(t)$$
 (17b)

Substituting these expressions, as well as Eq. (10), into Eq. (8) gives

$$m(\ddot{u} + \ddot{x}^{t}) = -\mu N \frac{1}{\sqrt{1 + [h'(u)]^{2}}} Z(t) - f_{c}(u, \dot{u}) - N \frac{h'(u)}{\sqrt{1 + [h'(u)]^{2}}}$$
(18a)

$$m(\ddot{v} + \ddot{y}^t) + mg = -\mu N \frac{h'(u)}{\sqrt{1 + [h'(u)]^2}} Z(t) + N \frac{1}{\sqrt{1 + [h'(u)]^2}}$$
(18b)

By substituting Eq. (5) as well as rearranging terms, Eq. (18) becomes

$$m\ddot{u} + \mu\lambda Z(t) + \lambda h'(u) = -m\ddot{x}^t - f_c(u, \dot{u})$$
(19a)

$$mh'(u)\ddot{u} + \mu\lambda h'(u)Z(t) - \lambda = -m\ddot{y}^t - mg - mh''(u)\dot{u}^2$$
(19b)

Eq. (19) represents a system of differential-algebraic equations [39] in terms of two unknowns— $\ddot{u}$  (differential) and  $\lambda$  (algebraic). These equations are linear in the two unknowns, so they can be written as follows:

$$\begin{bmatrix} 1 & \mu Z(t) + h'(u) \\ h'(u) & \mu h'(u) Z(t) - 1 \end{bmatrix} \begin{Bmatrix} m\ddot{u} \\ \lambda \end{Bmatrix} = \begin{Bmatrix} -m\ddot{x}^t - f_c(u, \dot{u}) \\ -m[\ddot{y}^t + h''(u)\dot{u}^2 + g] \end{Bmatrix}$$
(20)

This equation is coupled to the PS in Section 2.4, but first the nonlinear FIS force is discussed in the next section.

# 2.2. Nonlinear FIS force

From Eq. (19a), the horizontal force of the FIS can be derived as

$$f_{\text{FIS}} = \mu N \frac{1}{\sqrt{1 + [h'(u)]^2}} Z(t) + f_c(u) + N \frac{h'(u)}{\sqrt{1 + [h'(u)]^2}}$$
(21)

The first term in Eq. (21) is the frictional component of the FIS where  $\mu$  is the friction coefficient between the bearing and the curved track. The normal force, N, changes depending on the displacement of the FIS. The dimensionless hysteretic parameter Z(t) is described by the nonlinear differential equation shown in Eq. (15), and  $s_y$  denotes the yield displacement of the FIS. It is worth noting that this friction model does not include static friction, which would need to be overcome before the FIS can begin to displace; however, the Bouc-Wen model does sufficiently capture the nonlinear dynamics of interest here. The second term in Eq. (21) represents the contact force, and the last term corresponds to the gravitational restoring force of the FIS. In this study, a circular sliding/rolling profile is considered. For the case of a circular profile, the height, slope, and curvature are given by

$$h(u) = R - \sqrt{R^2 - u^2}, \ h'(u) = \frac{u}{\sqrt{R^2 - u^2}}, \ h''(u) = \frac{R^2}{(R^2 - u^2)^{3/2}}$$
 (22)

where R is the radius.

## 2.3. Primary Structure (PS)

The PS used in this study is a three-story shear building, which can be modeled as a 3 degrees of freedom system. The equation of motion of the PS is given by

$$\mathbf{M}\ddot{\mathbf{x}}(t) + \mathbf{C}\dot{\mathbf{x}}(t) + \mathbf{K}\mathbf{x}(t) = -\mathbf{M}\mathbf{1}\ddot{u}_{\varrho}(t)$$
(23)

where  $\mathbf{x}(t)$  is the vector of floor horizontal displacements, and  $\mathbf{M}$ ,  $\mathbf{C}$ , and  $\mathbf{K}$  are  $3 \times 3$  mass, damping, and stiffness matrices, respectively. The mass and stiffness matrices are given by

$$\mathbf{M} = \begin{bmatrix} m_1 & 0 & 0 \\ 0 & m_2 & 0 \\ 0 & 0 & m_3 \end{bmatrix}, \quad \mathbf{K} = \begin{bmatrix} k_1 + k_2 & -k_2 & 0 \\ -k_2 & k_2 + k_3 & -k_3 \\ 0 & -k_3 & k_3 \end{bmatrix}$$

where  $m_i$  and  $k_i$  are the mass and stiffness of the *i*th floor and story, respectively. The damping matrix is defined based on modal damping:

$$\mathbf{\Phi}^{\mathrm{T}}\mathbf{C}\mathbf{\Phi} = \begin{bmatrix} 2\zeta_1\omega_1 & 0 & 0\\ 0 & 2\zeta_2\omega_2 & 0\\ 0 & 0 & 2\zeta_3\omega_3 \end{bmatrix}$$
 (24)

where  $\zeta_i$  and  $\omega_i$  are the damping ratio and the frequency in the *i*th mode, and  $\Phi$  is the mass-normalized mode shape matrix. The quantities of these properties are detailed in Section 3.1. Vector **1** distributes the force coming from the horizontal ground acceleration  $\ddot{u}_g(t)$  to each of the floors.

## 2.4. The Coupled PS-FIS System

The total acceleration of the floor at the isolation system's location is given by

$$\ddot{\mathbf{x}}^{t}(t) = \mathbf{p}^{\mathrm{T}}(\ddot{\mathbf{x}}(t) + \mathbf{1}\ddot{\mathbf{u}}_{g}(t)) \tag{25}$$

where  $\mathbf{p}$  is a Boolean vector identifying the position of the FIS on the structure. By substituting this equation into Eq. (19a), the equation of motion of the FIS can be rewritten as

$$m\ddot{u}(t) + \frac{N}{\sqrt{1 + [h'(u)]^2}} [\mu Z(t) + h'(u)] + f_c(u, \dot{u}) = -m\mathbf{p}^{\mathrm{T}}(\ddot{\mathbf{x}}(t) + \mathbf{1}\ddot{u}_{\mathrm{g}}(t))$$
(26)

In this study, vertical displacement in the PS is neglected, so the vertical acceleration  $\ddot{y}^t$  imposed on the FIS by the PS is zero.

With the force of the FIS shown in Eq. (21), the dynamics of the coupled PS-FIS system is given by

$$\mathbf{M}\ddot{\mathbf{x}}(t) + \mathbf{C}\dot{\mathbf{x}}(t) + \mathbf{K}\mathbf{x}(t) = -\mathbf{M}\mathbf{1}\ddot{u}_{g}(t) + \mathbf{p}f_{FIS}(u, \dot{u}, \ddot{u})$$
(27a)

$$m\ddot{u}(t) + f_{\text{FIS}}(u, \dot{u}, \ddot{u}) = -m\mathbf{p}^{\text{T}}(\ddot{\mathbf{x}}(t) + \mathbf{1}\ddot{u}_{g}(t))$$
(27b)

From Eq. (27b),  $f_{FIS}$  can be expressed as

$$f_{\text{FIS}}(u, \dot{u}, \ddot{u})x = -m[\ddot{u}(t) + \mathbf{p}^{\text{T}}(\ddot{\mathbf{x}}(t) + \mathbf{1}\ddot{u}_{g}(t))]$$
(28)

Substituting this relationship to Eq. (27a), it can be re-expressed as

$$(\mathbf{M} + m\mathbf{p}\mathbf{p}^{\mathrm{T}})\ddot{\mathbf{x}}(t) + \mathbf{C}\dot{\mathbf{x}}(t) + \mathbf{K}\mathbf{x}(t) = -m\mathbf{p}\ddot{u}(t) - (\mathbf{M} + m\mathbf{p}\mathbf{p}^{\mathrm{T}})\mathbf{1}\ddot{u}_{g}(t)$$
(29)

Therefore, variables  $\ddot{\mathbf{x}}(t)$ ,  $\ddot{u}(t)$ ,  $\lambda(t)$ , and  $\dot{Z}(t)$  can be simultaneously solved from Eqs. (29), (20), and (15), which can be expressed in a matrix form as follows:

$$\begin{bmatrix} (\mathbf{M} + m\mathbf{p}\mathbf{p}^{\mathrm{T}}) & m\mathbf{p} & \mathbf{0}_{3\times 1} & \mathbf{0}_{3\times 1} \\ m\mathbf{p}^{\mathrm{T}} & m & \mu Z(t) + h'(u) & 0 \\ \mathbf{0}_{1\times 3} & mh'(u) & \mu h'(u)Z(t) - 1 & 0 \\ \mathbf{0}_{1\times 3} & 0 & 0 & 1 \end{bmatrix} \begin{pmatrix} \ddot{\mathbf{x}}(t) \\ \ddot{u}(t) \\ \dot{Z}(t) \end{pmatrix} =$$

$$\begin{cases}
-\mathbf{C}\dot{\mathbf{x}}(t) - \mathbf{K}\mathbf{x}(t) - (\mathbf{M} + m\mathbf{p}\mathbf{p}^{\mathrm{T}})\mathbf{1}\ddot{u}_{g}(t) \\
-m\ddot{u}_{g}(t) - f_{c}(u, \dot{u}) \\
-m[h''(u)\dot{u}^{2} + g] \\
\dot{u}(t)\sqrt{1 + [h'(u)]^{2}}\{A - [\beta \operatorname{sgn}(Z(t)\dot{u}(t)) + \gamma] |Z(t)|^{n}\}/s_{y}
\end{cases} (30)$$

The system consists of nine states comprised of six states for the displacement  $\mathbf{x}(t)$  and velocity  $\dot{\mathbf{x}}(t)$  of each floor in the PS, two states for FIS displacement u(t) and velocity  $\dot{u}(t)$ , and one state for the hysteretic displacement Z(t). Using MATLAB (R2019A, Mathworks, Natick, MA), Eqs. (30) and (15) are solved by utilizing the ODE built-in solver ode45 [40, 39]. This solver was selected because it utilizes an adaptive time stepping algorithm, which can help ensure that the nonlinear, piecewise dynamics are properly captured. The interval of integration (tspan) is set from zero to the final time with an increment of 0.001 sec, i.e., tspan = 0:0.001:tf where tf is the earthquake duration. The initial conditions are set as a vector of zero. The relative tolerance (RelTol) and absolute tolerance (AbsTol) are taken to be  $10^{-4}$  and  $10^{-7}$ , respectively, so as to achieve acceptable accuracy. All other values in this numerical integration are taken to be default. Greater computational efficiency could be achieved through the use of event location [41], for example state event location algorithm [42], but this is a topic of future research.

## 2.5. Performance Metrics

The performance evaluation of the dual-mode FIS is divided into two categories based on the intensity of the GM. For low-intensity GMs (those with intensity scale factors below impact), the evaluation concerns the *isolation* performance of the FIS. This is considered when the system displaces within its allowable capacities and behaves as a linear system. For high-intensity GMs (those with intensity scale factors above impact), the evaluation concerns the *absorption* performance of the PS. This is considered when the system displaces more than its allowable capacity, thus creating an impact that results in a highly nonlinear response. The *dual-mode* FIS performance is evaluated experimentally for different gaps  $u_o$  with details described in Section 3.2.

In the case of the isolation performance, the response quantity of interest is the peak absolute acceleration of the FIS:

$$a_{\text{FIS}}^{\text{max}} = \max_{t} |a(t)| \tag{31}$$

where  $a(t) \equiv \ddot{u}_g(t) + \mathbf{p}^T \ddot{x}(t) + \ddot{u}(t)$  is the absolute acceleration of the FIS. To evaluate the isolation performance,  $a_{\text{FIS}}^{\text{max}}$  is then compared to the second story's acceleration  $(a_2)$  for the case of no FIS  $(a_2^{\text{no FIS}})$  and locked FIS  $(a_2^{\text{locked}})$ . The isolation performance is also indicated by the normalized isolation performance index  $(J_a)$ , which is defined as

$$J_a = \frac{a_{\text{FIS}}^{\text{max}}}{a_2^{\text{locked}}} \tag{32}$$

Note that later figures showing  $J_a$  will also includes the case of  $a_2^{\text{no FIS}}$  being normalized by  $a_2^{\text{locked}}$ . Of secondary interest is the peak displacement of the FIS relative to the structure level:

$$u^{\max} = \max_{t} |u(t)| \tag{33}$$

where u(t) is the relative displacement across the isolation layer.

In the case of the absorption performance, the response quantity of interest is the peak inter-story drift ratio:

$$\delta_i^{\max} = \max_t |d_i(t)/h_i| \tag{34}$$

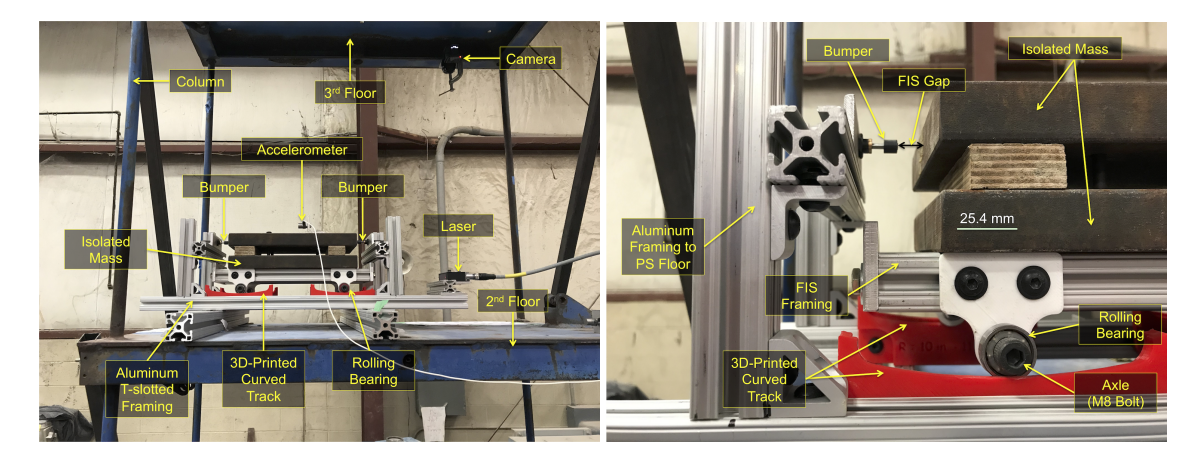


Figure 3: Experimental floor isolation system (FIS) installed on the second floor of the primary structure (PS)

where  $d_i(t)$  and  $h_i$  are the inter-story drift and height of the *i*th story respectively, and  $\delta_i^{\max}$  is the maximum inter-story drift ratio of the associated story. To evaluate the absorption performance,  $\delta_i^{\max}$  is then compared to each story's inter-story drift ratio for the case of no FIS ( $\delta_i^{\text{no FIS}}$ ) and locked FIS ( $\delta_i^{\text{locked}}$ ). The absorption performance is also indicated by the normalized absorption performance index ( $J_{\delta}$ ) which is defined as

$$J_{\delta} = \frac{\delta_{1}^{\text{max}}}{\delta_{1}^{\text{locked}}} \tag{35}$$

The first stories drift  $(\delta_1)$  is considered because the inter-story drift of the first floor is typically largest. Note that later figures showing  $J_{\delta}$  also includes the case of  $\delta_1^{\text{no FIS}}$  being normalized by  $\delta_1^{\text{locked}}$ .

## 3. Experimental Setup and Protocol

To evaluate the performance of the proposed dual-mode FIS, a PS-FIS system was experimentally tested at Donald G. Fears Structural Engineering Laboratory at the University of Oklahoma. Details of the experimental system and testing protocol are described here, but a more comprehensive description including the experimental data is available in Refs. [43, 44].

## 3.1. Primary Structure (PS)

The PS used in this experimental approach is a lab-scale, three-story, shear-type structure. The columns of the structure are made of high yield strength spring steel, and its base is attached to a shake table in fixed connection; the structure is braced in the transverse direction, allowing displacement in only one direction. Each floor of the PS is about 56 kg, with slightly more mass (3.8 kg) on the 2nd floor coming from the aluminum framing. The 1st, 2nd, and 3rd story stiffnesses are 113, 136, and 158 N/mm, respectively. The modal frequencies (damping ratios) of the PS were identified to be 3.3 Hz (0.10%), 9.8 Hz (0.1%), and 14.4 Hz (0.20%) [43].

# 3.2. Floor Isolation System (FIS)

The FIS used in this experiment is shown in Fig. 3, which was installed on the 2nd floor of the PS. An isometric view of the setup is shown in Fig. 4, along with the relevant dimensions. The FIS consists of four rolling bearings that roll on the 3D-printed curved tracks [45] each having a 265-mm radius of curvature,

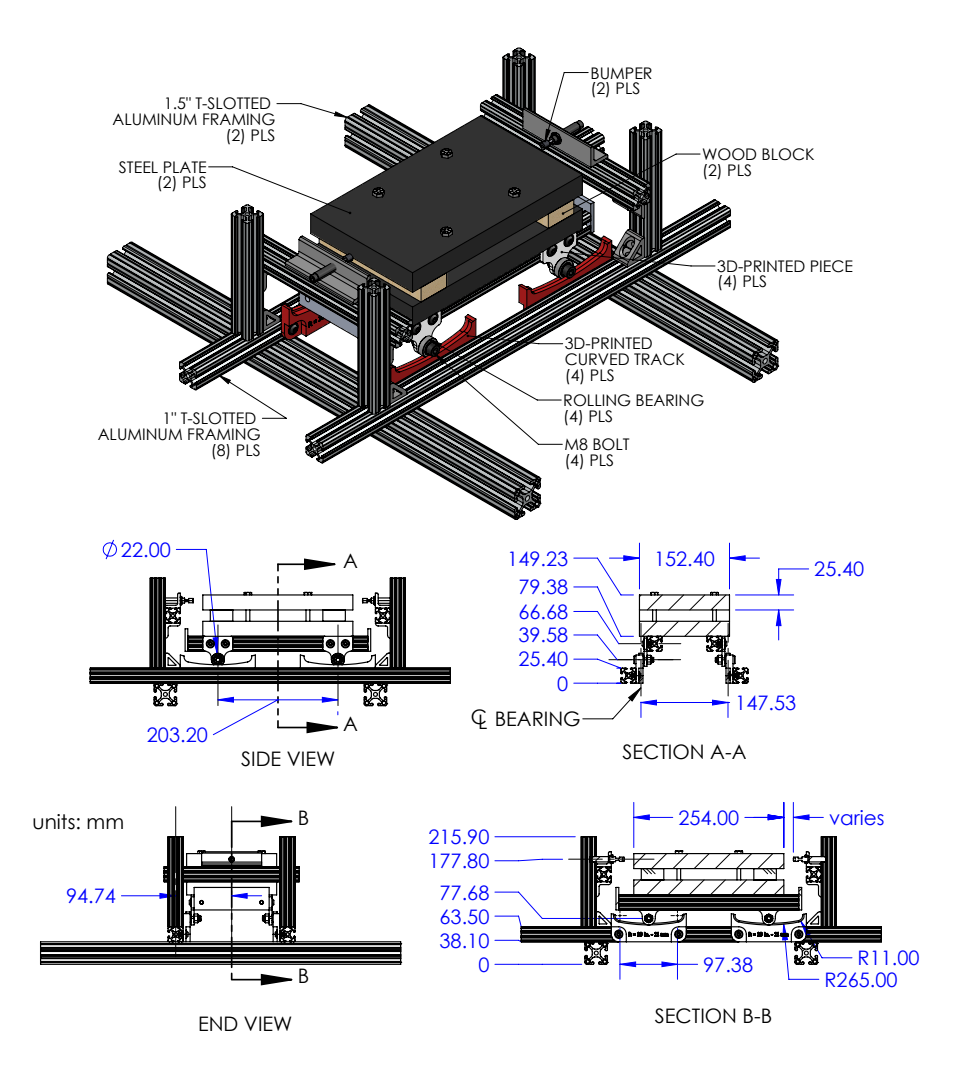


Figure 4: Isometric, side, and end views of FIS setup

which corresponds to a 1-s isolation period. The isolated equipment is represented by two steel blocks that constitute a total mass of 9 kg, which is equivalent to about 15% of the 2nd floor's mass and 5.2% of the PS's total mass. This is comparable to mass ratios considered by others for secondary systems [29, 28, 36, 25].

To create nonlinearity in the system, the FIS is designed to gradually impact with two bumpers (characterized in Section 3.3), installed on either side of the FIS as shown in Figs. 3 and 4. Miniature shock absorbers (MC25, Ace Controls Inc., Farmington Hills, MI, USA) were selected based on their energy capacity for this application. These bumpers have a 6.6-mm stroke that allows for an additional compression during impact. Therefore, for clarification, gap  $u_o$  is measured from the FIS's equilibrium position to the first touch when the isolated mass engages with the bumper.

To see how displacement capacity affects the performance of the dual-mode FIS, three gaps are considered, which are given in Table 1. Gap B serves as the baseline case, about which gaps C and F are selected. Gaps C and F are respectively smaller and larger than gap B by about 50%.

As mentioned in Section 2.5, performance evaluation of the dual-mode FIS with gaps B, C, and F are compared to the cases of *no FIS* and *locked FIS*. The former refers to the case where the FIS is removed

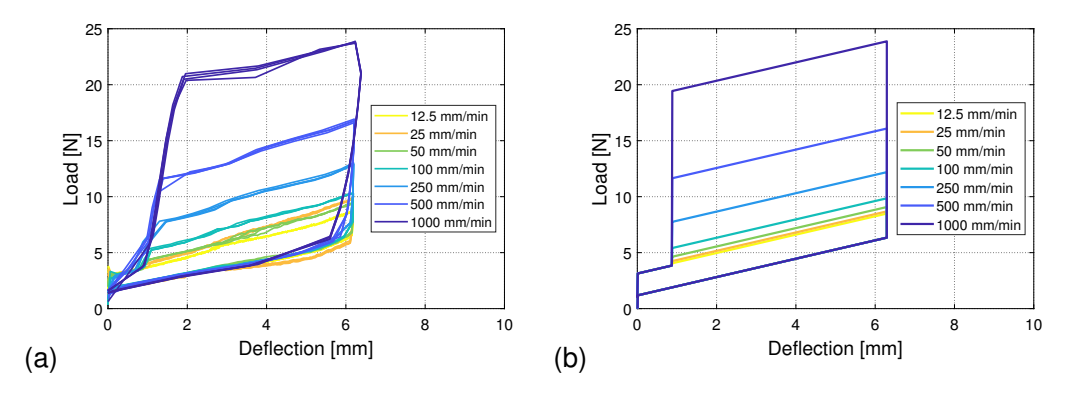


Figure 5: Load-deflection curves based on (a) experimental data and (b) estimated contact force  $f_c$  model

from the second floor of the PS. The latter refers to the case where the FIS is not allowed to move, i.e., the gap is equivalent to zero.

#### 3.3. Bumper

One of the miniature shock absorbers used as bumpers in the FIS was characterized using load-deflection tests at loading rates of 12.5, 25, 50, 100, 250, 500, and 1000 mm/min. Fig. 5(a) shows the experimentally measured load-deflection curves, where deflection represents the depression of the shock absorber.

From these tests, the contact force  $f_c$  model was parameterized as follows:

$$f_c(u, \dot{u}) = \{k_1[u - u_o \operatorname{sgn}(u)] + f_o \operatorname{sgn}(u) + f_f \operatorname{sgn}(\dot{u})\} \times \mathbb{I}_{|u| \geqslant u_o} + c\dot{u} \times \mathbb{I}_{u\dot{u} \geqslant 0} \times \mathbb{I}_{|u| \geqslant u_o + u_1} + k_2[u - (u_o + u_2) \operatorname{sgn}(u)] \times \mathbb{I}_{|u| \geqslant u_o + u_2}$$
(36)

where  $sgn(\cdot)$  is the signum function, and  $\mathbb{I}_{(\cdot)}$  is the indicator function. The model parameters were identified to be  $k_1 = 0.8205$  N/mm,  $f_o = 2.154$  N,  $f_f = 0.9776$  N, c = 0.935 N·s/mm,  $u_1 = 0.88$  mm,  $k_2 = 50$  N/mm, and  $u_2 = 6.3$  mm. Fig. 5(b) shows the fitted load-deflection curves, which show good agreement with the experiments (Fig. 5(b)).

## 3.4. Instrumentation

The experimental setup of the PS-FIS system is shown in Fig. 6. Five accelerometers (352C33, PCB Piezotronics, Inc., Depew, NY) are installed to measure the acceleration of the ground, first floor, second floor, third floor, and the FIS. A laser (optoNCDT 1302, Micro-Epsilon, Ortenburg, Germany) measured the displacement of the FIS relative to the 2nd floor. To measure the inter-story drift of each story, a vision-based technique [46, 47] was used; three cameras (HERO Session, GoPro, Inc., San Mateo, CA) were installed on the undersides of the floors. Inter-story drift of each story was determined from the tracked movement of high-contrast grids on the floor below. Note, the three cameras acquired video asynchronously with each other, and with the other data acquisition systems, but synchronization was not critical because peak

Table 1: FIS gaps  $u_o$  used for experimental FIS

	Gap		
	В	С	F
FIS gap $u_o$ [mm]	21.95	11.95	32.79

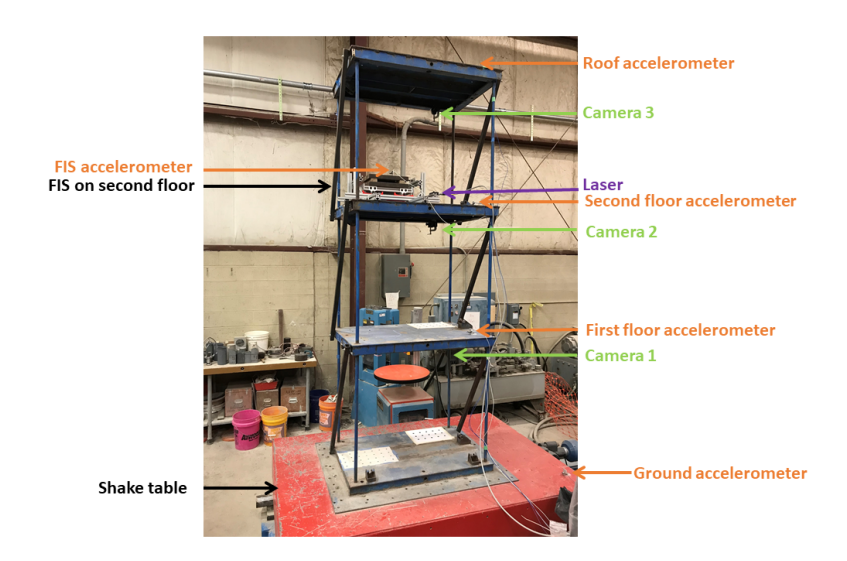


Figure 6: Experimental setup of PS-FIS system

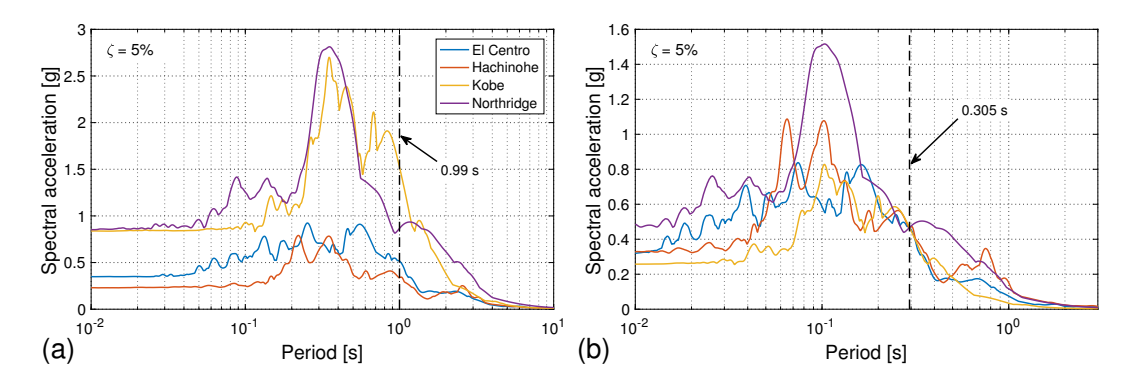


Figure 7: Response spectra of (a) unscaled GMs and (b) scaled GMs with an intensity scale factor of 1.0.

responses were of greatest interest. The accelerometers, laser, and cameras used sampling rates of 2000 Hz, 750 Hz, and 100 fps, respectively.

## 3.5. Experimental Protocol

For the experiments, four historic GMs—El Centro, Hachinohe, Kobe and Northridge—are used based on the recommendation of Ref. [48]. The 5%-damped response spectra for the unscaled records are shown in Fig. 7(a). Three types of scale factors have been applied to the recorded GMs in order to generate the labscale GMs. These include scale factors for response spectral matching, similitude, and GM intensity. First, the GMs have been scaled to have a 1-s, 5%-damped spectral acceleration of 0.2g. Then, for similitude, the earthquake's amplitude and time are scaled using the benchmark building [48] as a reference structure. The reference structure has a fundamental frequency of 0.99 Hz while that of the lab prototype is 3.3 Hz, so the time scale factor is 3.4. The benchmark building has a story height of 396 cm and that of the prototype is 79.4 cm, so the length scale factor is 5.0. Finally, since the performance of the dual-mode FIS is evaluated based on GM intensity, an additional scale factor has been applied such that the FIS can be tested from low-intensity GMs to high-intensity GMs. The range of the intensity scale factor is different for each GM depending on amplitude of the PS response, which can be estimated visually from the PS responses

observed during testing. The intensity scale factors for each GM are given in Table 2 for the different FIS configurations tested. These intensity scale factors are selected to cover a reasonable range of data points prior to and after impacts for each GM. Fig. 7(b) shows the 5% damped response spectra for the scaled GMs with an intensity scale factor of 1.0.

## 4. Experimental Results

This section discusses the experimental results and evaluates the dual functionality of the FIS. To recall, the isolation performance is determined by evaluating the maximum acceleration of the FIS ( $a_{\rm FIS}^{\rm max}$ ) and the second floor ( $a_2^{\rm locked}$ ). On the other hand, the absorption performance is determined by evaluating the interstory drifts of the first, second and third floor denoted by  $\delta_1$ ,  $\delta_2$  and  $\delta_3$  respectively. The case of locked FIS serves as a baseline performance for evaluating the cases with gaps, although the case of no FIS has also been included in the results.

Since the dual-mode FIS performs differently when subjected to different earthquakes, each GM is evaluated individually containing the discussion of their baseline performance, isolation performance and absorption performance. Note that "scale factor" or "GM scale factor" in this section refers to the intensity scale factor.

Table 2: Experimental tests conducted. Impacts were observed at intensity scale factors that are italicized.

Configuration	GM	Intensity scale factor
No FIS	El Centro Hachinhoe Kobe Northridge	0.5, 1, 2, 3 0.5, 1, 1.5 0.5, 1, 2, 3 0.5, 1, 1.5, 2
Locked FIS	El Centro Hachinohe Kobe Northridge	0.5, 1, 2, 3 0.5, 1, 1.5 0.5, 1, 2, 3 0.5, 1, 1.5, 2
Gap B	El Centro Hachinohe Kobe Northridge	0.25, 0.5, 0.75, 1, 1.25, 1.5, 1.75, 2, 2.25, 2.5 0.125, 0.25, 0.375, 0.5, 0.75, 1, 1.25, 1.5 0.25, 0.5, 0.75, 1, 1.25, 1.5, 1.75, 2, 2.25, 2.5, 2.75, 3 0.25, 0.375, 0.5, 0.625, 0.75, 1, 1.25, 1.5, 1.75, 2
Gap C	El Centro Hachinohe Kobe Northridge	0.125, 0.25, 0.375, 0.5, 0.625, 0.75, 0.875, 1, 1.25, 1.5, 1.75, 2 0.125, 0.25, 0.375, 0.5, 0.625, 0.75, 1, 1.25 0.125, 0.25, 0.375, 0.5, 0.625, 0.75, 1, 1.25, 1.5, 1.75, 2 0.125, 0.25, 0.375, 0.5, 0.625, 0.75, 1, 1.25, 1.5
Gap F	El Centro Hachinohe Kobe Northridge	0.5, 0.75, 1, 1.25, 1.5, 1.75, 2, 2.25 0.25, 0.375, 0.5, 0.625, 0.75, 1, 1.25, 1.5 0.5, 1, 1.5, 1.75, 2, 2.25 0.25, 0.5, 0.75, 1, 1.25, 1.5, 1.75, 2

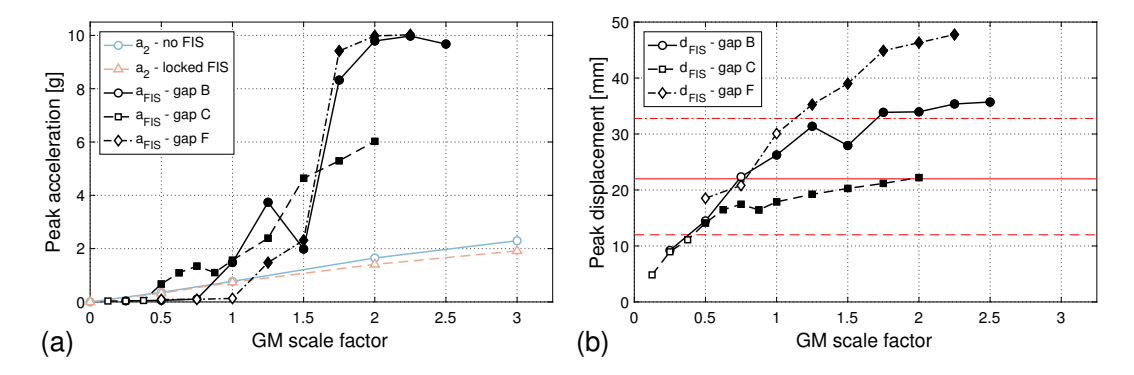


Figure 8: Experimental peak FIS responses for El Centro: (a) total accelerations  $a_2$  and  $a_{\text{FIS}}$ , and (b) FIS displacement  $d_{\text{FIS}}$ . The horizontal lines represent the FIS gap for each case (based on line style). The filled markers indicates cases in which impacts occurred in FISs with different gaps.

## 4.1. Baseline (linear) performance

Figs. 8(a) and 9 show the response of the PS with no FIS and the locked FIS when subject to El Centro at varying scale factors. The 2nd floor's peak total acceleration (Fig. 8(a)) and the peak inter-story drift ratios (Fig. 9) exhibit approximately linear responses over the range of scale factors considered. In nearly all cases, larger peak accelerations and inter-story drifts are seen for the case of no FIS. Similar observations concerning linearity and peak responses were observed for the other GMs, which are not shown here due to space limitations but are available in Ref. [43]. These linear PS responses serve as the baseline to which the isolation and absorption performance of the dual-mode FIS are compared in the following sections.

Note that although a scale factor of zero was not tested (see Table 2), these points have been included for the cases of no FIS and locked FIS in Figs. 8(a) and 9 assuming a peak response value of zero.

## 4.2. Isolation performance

Fig. 8 shows peak responses of the FIS with different gaps—B, C, and F—at varying scale factors when subjected to El Centro. Total acceleration and displacement of the FIS are shown in Figs. 8(a) and 8(b), respectively.

For the acceleration response (Fig. 8(a)), when compared to the baseline case (locked FIS), there is always a decrease in acceleration prior to impact (open markers) for all three gaps. At a scale factor of 0.5, gaps B and F exhibit a decrease in acceleration with respect to the locked FIS of about 82% and 72%, respectively. Gap C also experiences a reduction in acceleration before it impacts. Therefore, prior to impact, the FIS performs well as an isolator when subjected to El Centro. However, when impacts occur (filled markers), the data tells a different story. A dramatic rise in acceleration can be observed for all cases. Gap B experiences an increase in FIS acceleration about twice as much the baseline case at a scale factor of 1. Similar observation can be made during impact for gaps C and F. After the first impact occurs, the system continues to gain acceleration as the scale factor increases. Therefore, during and after impact, the performance of the FIS as an isolator degrades, during which time the experimental evaluation shifts to look at the PS responses instead as discussed in Section 4.2.1.

For the FIS displacement response (Fig. 8(b)), notice that the three horizontal lines corresponding to the FIS gaps are below each gap's impact scale factor, which means gaps B, C and F indeed impact at a scale factor of 1, 0.5 and 1.25, respectively. As shown in Fig. 8(b), the displacement of the FIS continues to increase even though it has already reached its allowable displacement capacity. This is due to the aforementioned additional compression of 6.6 mm in the bumpers. However, the ultimate displacement

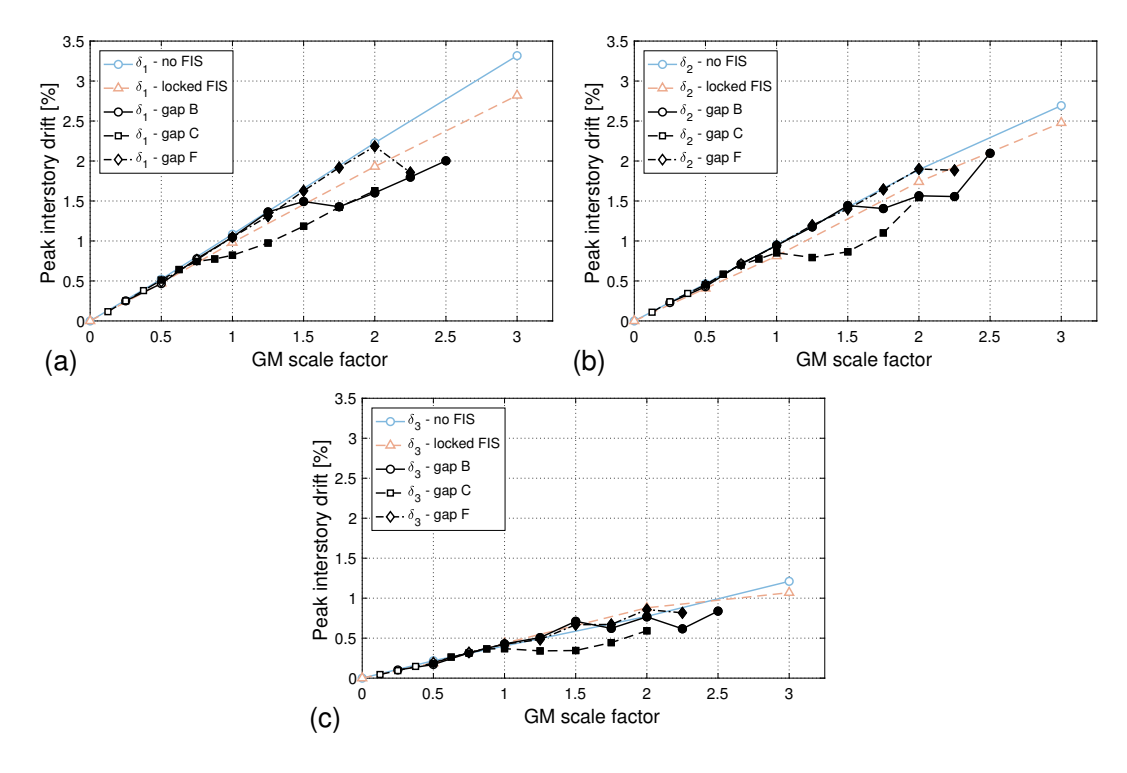


Figure 9: Experimental peak PS responses for El Centro: (a) 1st story drift  $\delta_1$ , (b) 2nd story drift  $\delta_2$ , and (c) 3rd story drift  $\delta_3$ . The filled markers indicates cases in which impacts occurred in FISs with different gaps.

goes beyond the addition of 6.6 mm, which means there has to be an additional deflection in the system. This could be due to the way the bumpers are installed during testing. As seen in Fig. 3, the bumpers are located at the end of a cantilever (from the aluminum support), and thus deflects when strongly hit by the top steel plate. This phenomenon can also be seen in other GM cases.

In summary, when subjected to El Centro, the FIS indeed shows good isolation performance prior to impact. Similar results for isolation performance were observed for the other GMs [43].

## 4.2.1. Absorption performance

Fig. 9 shows peak responses of the PS with different gaps at varying scale factors when subjected to El Centro. Prior to impact (open markers), it is apparent that the drift responses for the cases with FIS are almost the same as the case of no FIS. Therefore, the FIS has no effect on the responses of the PS when it displaces within the allowable clearance (gap). However, after impact (filled markers), a divergence from the linear response (no FIS) can be observed for all three stories. The greatest divergence is observed for gap C where the reduction seems greatest at a scale factor of 1.5. This gap, though having a smaller capacity, seems to outperform gaps B and F for the absorption performance. While gaps B and F also exhibit interstory drift reduction, notice that their divergence occur at higher scale factors compared to gap C because they have larger gaps and need higher intensity scale factors to see impacts. Among the three stories, gap B shows the best reduction in the first story while its performance in the second and third stories is variable. Even though gap F has seismic displacement capacity 50% larger than gap B, it seems to perform worse than gaps B and C overall. After impact, gap F continues to show increase in drift until a scale factor of 2, but eventually exhibits a reduction at a scale factor of 2.25.

For all gaps, a reduction in inter-story drift does not occur immediately after first impact. Noticeable

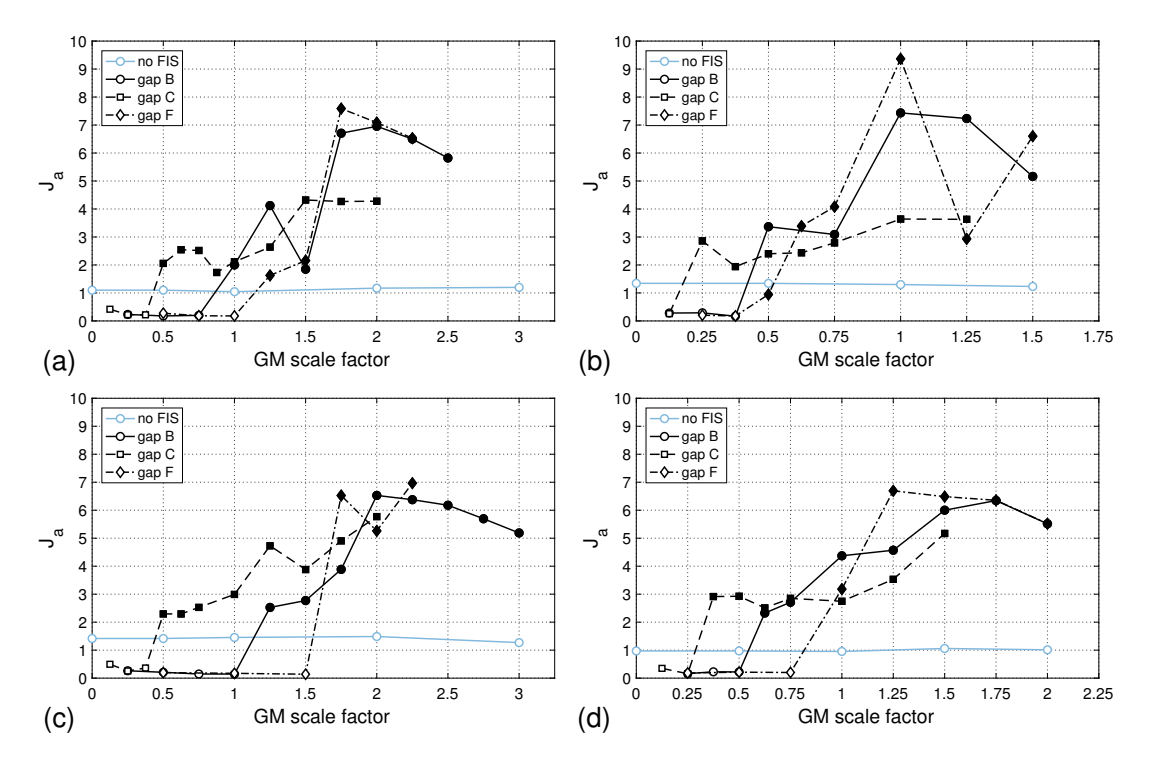


Figure 10: Experimental peak total acceleration performance index  $J_a$  for (a) El Centro, (b) Hachinohe, (c) Kobe, and (d) Northridge. The filled markers indicates cases in which impacts occurred in FISs with different gaps.

divergence seems to happen at a higher scale factors where the impact is stronger. Recall that gaps B and C have the greatest increase in FIS acceleration from a scale factor of 1.5 to 1.75 (see Fig. 8(a)). At this intensity, gap B also exhibits its first reduction in drift as shown in Fig. 9, which mean harsh impact is good for the absorption performance of gap B. However, gap F continues to show increase in inter-story drift despite experiencing similar acceleration gain at a scale factor of 1.5. For gap C, a similar observation to gap B can be observed where it shows great absorption performance within the intensity range in which it has high accelerations.

In summary, when subjected to El Centro, the FIS indeed shows absorption performance after impact. However, this performance varies for different FIS gaps. Similar conclusions for absorption performance can be made for the other GMs [43].

# 4.3. Normalized Performance Indices

The isolation and absorption performances of the dual-mode FIS can also be evaluated by the normalized isolation performance index  $J_a$  and normalized absorption performance index  $J_\delta$ , respectively, as defined in Section 2.5. These performance indices are shown in Figs. 10 and 11 for all four GMs. Note that different GM scale factors were used for each configuration (see Table 2), so the normalizing peak responses ( $a_2^{\text{locked}}$  and  $\delta_1^{\text{locked}}$ ) were found by interpolating between the tested cases for the locked FIS configuration. Although a scale factor of zero was not tested (see Table 2) for the cases of no FIS and locked FIS, these points have been included for the no FIS configuration in Figs. 10 and 11 assuming the  $J_a$  or  $J_\delta$  value for the lowest scale factor that was tested.

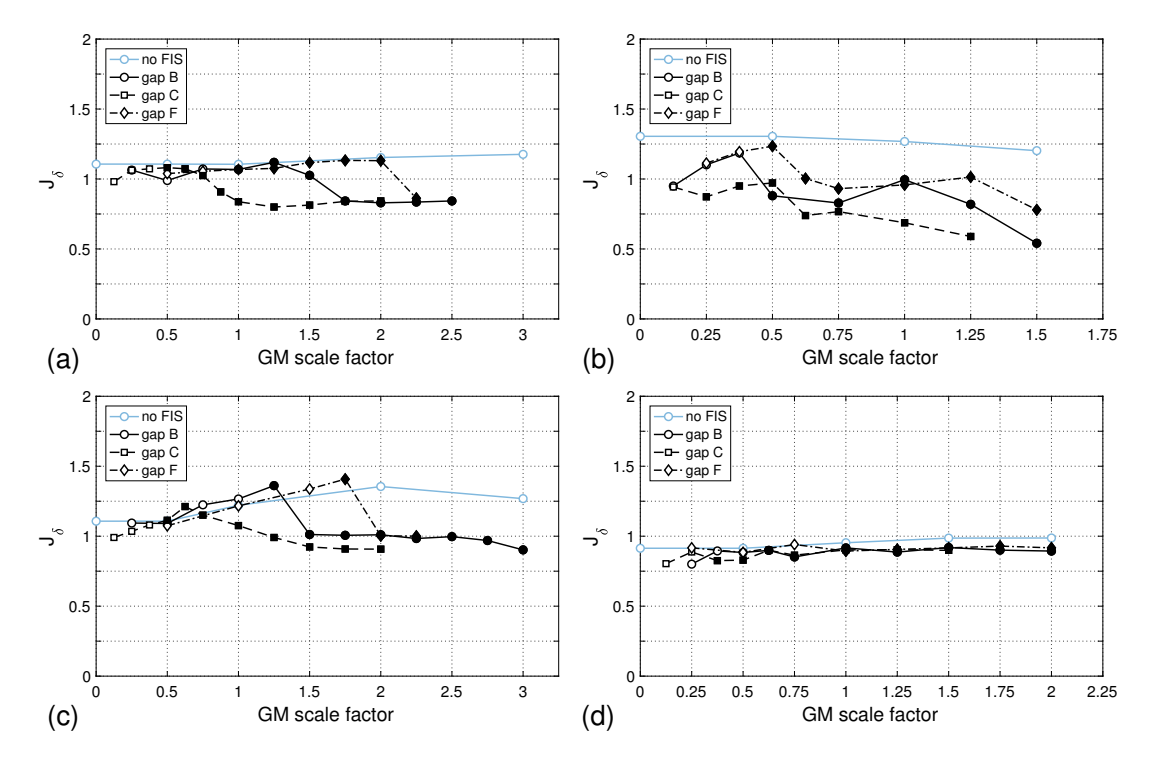


Figure 11: Experimental peak interstory drift performance index  $J_{\delta}$  for (a) El Centro, (b) Hachinohe, (c) Kobe, and (d) Northridge. The filled markers indicates cases in which impacts occurred in the FIS.

#### 4.3.1. Isolation Performance

Fig. 10 shows the normalized isolation performance index for the cases with no FIS and with gaps B, C, and F when subjected to different GMs at varying scale factors. Note that since these values are normalized by  $a_2^{\rm locked}$ , points below 1 indicate good isolation performance relative to the locked FIS case, whereas points above 1 indicate poor isolation performance relative to the locked FIS case. For El Centro, Hachinohe, and Kobe, the case of no FIS lies above 1, indicating that the addition of mass to the second floor (i.e., locked FIS) reduces the second floor's acceleration. This change in acceleration is attributed to the local sensitivity of these GMs' response spectra in the vicinity of the fundamental mode of the linear PS with and without the additional mass. However, this is not the case for Northridge, since the case of no FIS stays nearly at a value of 1.

For gaps B, C, and D, excellent isolation performance is observed prior to impacts for all GMs. However, for scale factors producing impacts, the FIS performs poorly as an isolator due to a drastic increase in peak accelerations as shown in Fig. 10. Notice that while gap F can generally isolate at higher intensity scale factors, it also exhibits the greatest gain in acceleration after impact. This is because the larger gap allows for greater velocities to develop before impact, resulting in harsher impacts with higher accelerations.

## 4.3.2. Absorption Performance

Fig. 11 shows the normalized absorption performance index for the cases with no FIS and with gaps B, C, and F when subjected to different GMs at varying scale factors. Since these values are normalized by  $\delta_1^{\text{locked}}$ , points below 1 indicate good absorption performance relative to the locked FIS case, whereas points above 1 indicate poor absorption performance relative to the locked FIS case. For the no FIS configuration, increased drifts ( $J_{\delta} > 1$ ) are observed for El Centro, Hachinohe, and Kobe, whereas slightly reduced drifts

 $(J_{\delta} < 1)$  are observed for Northridge. As before with the acceleration, the difference in drifts between no FIS and locked FIS can be attributed to the local sensitivity of the response spectra in the vicinity of the fundamental mode with and without the additional FIS mass.

For FISs with gaps B, C, and F, the PS's inter-story drift response mimics that of the no FIS case, which is to be expected because the FIS effectively decouples the isolated mass from the PS. PS responses for El Centro, Hachinohe, and Kobe exhibit an increase in inter-story drift ( $J_{\delta} > 1$ ) prior to impact, while Northridge's response stays constant throughout where a small reduction in drift ( $J_{\delta} < 1$ ) can be observed both before and after impact. For scale factors inducing impact, El Centro and Kobe continue to show an increase in drift until a certain scale factor where drift reduction can be noticed. This delayed reduction in response can be attributed to a grazing bifurcation [49, 50, 51]. This contact behavior is notoriously hard to predict, and further may lead quite abruptly into chaos with increased forcing amplitude [51, 52, 53]. Dramatically different results are seen for El Centro, Hachinohe, and Kobe after impact, with  $J_{\delta}$  diverging from that of the no FIS case. El Centro and Hachinohe show the highest reduction in drift relative to the locked FIS ( $0.5 < J_{\delta} < 1$ , while Kobe appears to approach that of the locked FIS ( $J_{\delta} \approx 1$ ). Northridge has negligible effect overall on the absorption performance. For El Centro, Hachinohe, and Kobe, gap C seems most influential on the drift reduction. Overall, gap B outperforms gap F for the absorption performance. Notice that among these four GMs, Hachinohe exhibits the best absorption performance ( $J_{\delta}$  approaching 0.5), and the reasons accountable for such great performance are discussed below.

From earlier discussion, it is apparent that El Centro and Hachinohe provide good absorption performance whereas Kobe and Northridge have very little effect on the absorption performance of the FIS. This may be because El Centro and Hachinohe have relatively longer strong motion duration  $t_{\text{strong}}$  [54]—24.4 and 27.9 s, respectively, accounting for 90% of the Arias intensity  $I_a$  [55]—compared to Kobe (8.34 s) and Northridge (5.33 s), even though the latter two have higher peak ground acceleration values. For this reason, there is time for the absorbers to begin functioning, which results in a good absorption performance. Therefore, the longer strong motion duration can be the main reason why El Centro and Hachinohe exhibit greater absorption performance.

To further evaluate the GM characteristics in relation to the absorption performance, spectrograms of the measured roof accelerations for gap B are shown in Fig. 12 for Hachinohe and Kobe. The horizontal red streaks represent the amount of energy present in the PS's response for each GM. They appear at the frequencies of about 3.5, 10, and 15 Hz which correspond to the PS's natural frequencies. In both cases, a redistribution of energy from the first mode to higher modes can be seen. Due to the nature of higher mode's mode shape, it contributes less to the drift response of the PS. Therefore, a greater energy redistribution to higher modes corresponds to a smaller PS responses. Notice that Hachinohe overall has a relatively higher redistribution of energy to the third mode than as seen with Kobe (and other GMs not shown here), which can be another reason why it exhibits the best absorption performance.

## 4.4. Discussion of Transmitted Forces

It is worth noting that at the end of some of the series of tests, the vertical columns supporting the bumpers (see "Aluminum Framing to PS Floor" in Fig. 3) were seen to be permanently rotated. This was due to the considerable forces being transmitted during impact, especially when the shock absorber's 6.6-mm stroke was exceeded. Special care must be taken in the practical concern of detailing such impact-based devices [56] to ensure there is a sufficient load path to transmit these considerable forces without damaging the PS in the process. This is especially true when not insignificant mass ratios (e.g.,  $\sim$ 5% of the PS [57, 28, 29]) are considered.

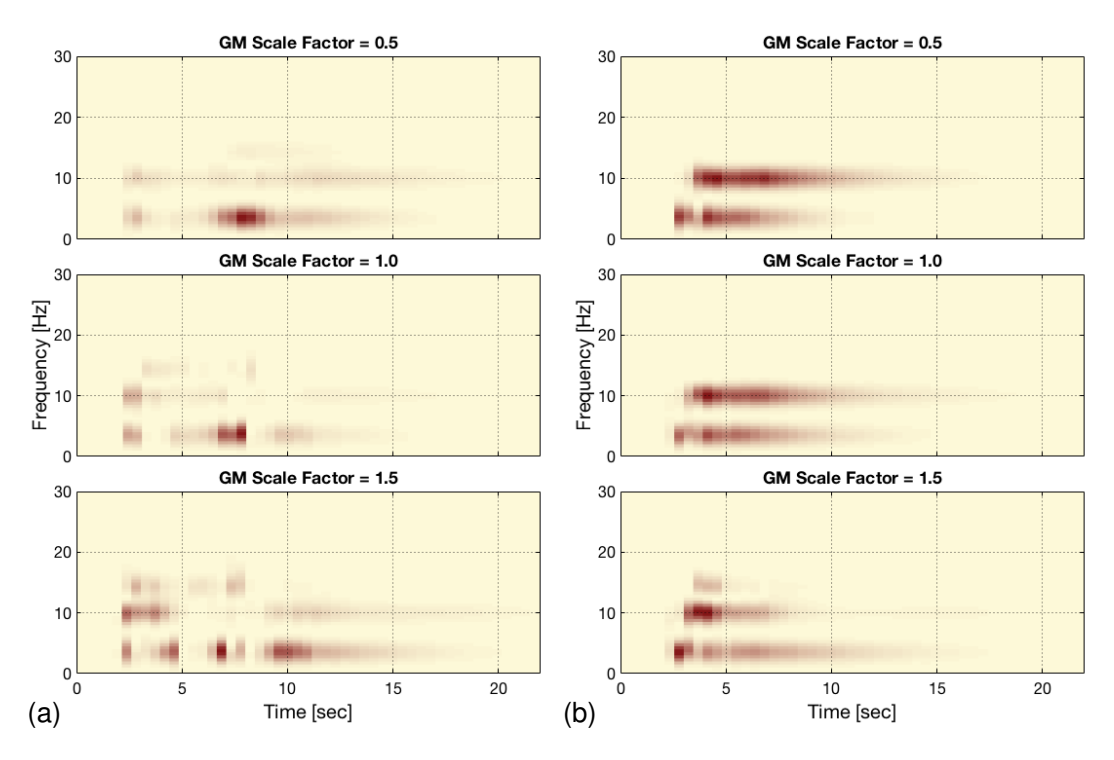


Figure 12: Spectrograms of the roof acceleration for gap B subject to (a) Hachinohe and (b) Kobe.

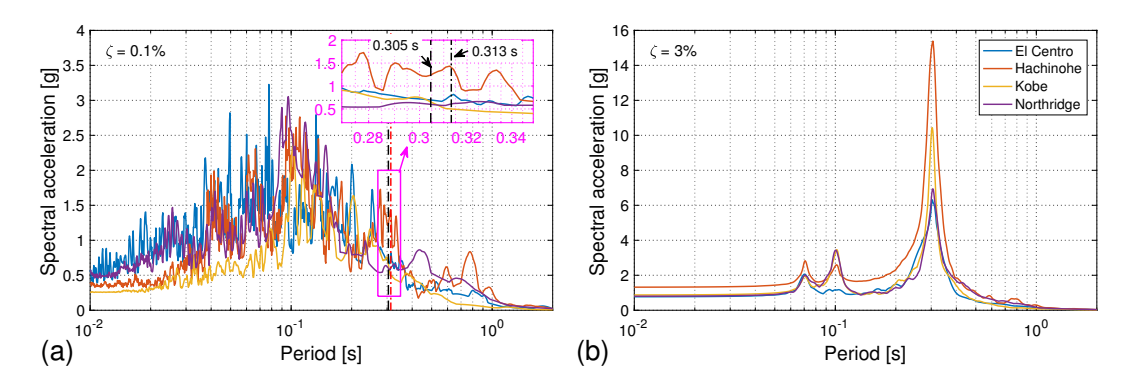


Figure 13: Response spectra of (a) scaled ground accelerations with an intensity scale factor of 1.0 and (b) 2nd floor total acceleration for PS with no FIS subject to scaled GMs with an intensity scale factor of 1.0.

## 5. Numerical Results

In this section, the PS-FIS system is numerically modelled using the same GMs and system properties discussed in Section 3. Fig. 13(a) shows the 0.1%-damped response spectra for the scaled GMs with an intensity scale factor of 1.0; 0.1% damping is used because this was the experimentally estimated damping in the PS's first mode (see Section 3.1). The inset shows a close up of the spectra near the PS's fundamental period (0.305 s) with no FIS, along with the fundamental period (0.313 s) of the PS with the FIS fixed. It is worth noting that El Centro and Hachinohe have larger responses at 0.313 s than at 0.305 s; the reverse is true for Kobe, and the spectral responses approximately equal at these two periods for Northridge.

For modeling the FIS, the form of the contact force  $f_c$  found in the characterization tests (Section 3.3) is used. The friction coefficient  $\mu$  and yield displacement  $s_y$  are taken to be 1% and 1 mm, respectively;

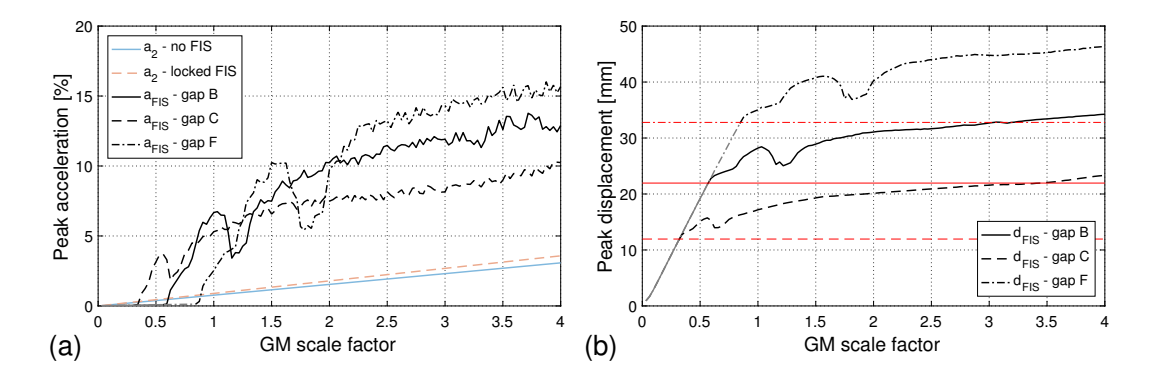


Figure 14: Numerical peak FIS responses with different gaps for El Centro: (a) total accelerations  $a_2$  and  $a_{FIS}$ , and (b) FIS displacement  $d_{FIS}$ . The horizontal lines represent the FIS gap for each case (based on line style). The gray portion indicates cases in which there are no impact whereas the black portion indicates cases in which impacts occurred in the FIS.

the Bouc-Wen parameters [58] A,  $\beta$ ,  $\gamma$ , and n are taken to be 1, 0.5, 0.5, and 2, respectively. These values were selected to give a reasonable representation of the rolling resistance in such a system [45]. Based on these values, the equivalent viscous damping ratio for a cyclic displacement  $u_o = 50$  mm at the FIS's natural period  $T_n = 1$  s can be approximated as  $\zeta \approx 2g\mu/[\pi(2\pi/T_n)^2u_o] = 3\%$ . Fig. 13(b) shows the 3%-damped floor response spectra at the 2nd floor of the PS with no FIS. As expected, the floor response spectra are dominated by the first mode (0.305 s) response, with less contribution from the 2nd (0.102 s) and 3rd (0.069 s) modes, even though there is energy at these periods in the ground motion spectrum (Fig. 13(a)).

With ease of numerical simulation, isolation and absorption performance of the FIS was evaluated at finer resolution of intensity scale factors. Using simulation, the numerical results are obtained and discussed in this section. The peak acceleration and interstory drift responses are plotted in the same format shown in the experimental results. Responses for El Centro are shown in Figs. 14 and 15. In interest of space, responses for the other GMs are not shown here, but can be found in Ref. [43]. These results contain overall features that resemble the experimental results (see Section 4) except for the baseline cases (no FIS and locked FIS) for El Centro and Hachinohe. From the experiment, the case of locked FIS for these two GMs exhibits lower responses than the case of no FIS. However, the reverse is seen in the numerical results. This discrepancy is due to the sensitivity of the response spectra in the vicinity of the fundamental mode of the PS with no FIS and locked FIS (see Fig. 13), as previously discussed. Baseline cases of Kobe and Northridge are accurately reflected in the numerical results. For the cases with FIS gaps, the responses contain the overall features exhibited in the experiment. For a quantitative comparison of the peak responses, Fig. 16 compares the results for El Centro with gap C. Good agreement is seen between the numerically predicted and experimentally measured FIS displacements  $d_{\rm FIS}$  (Fig. 16(b)) and first interstory drift  $\delta_1$  (Fig. 16(c)). The experimentally measured FIS accelerations  $a_{\rm FIS}$  (Fig. 16(a)) are lower than those numerically predicted, which may be attributed in part to the accelerometers missing the peak during the brief impact. Overall, acceptable agreement is observed prior to impact, but there is some divergence in the numerical and experimental responses, which is attributed to the challenge of predicting responses with impacts as previously noted.

The isolation and absorption performance indices are shown in Figs. 17 and 18, respectively. Recall that these data are normalized by the case of locked FIS. Therefore, values below 1 for  $J_a$  and  $J_\delta$  exhibit enhanced performance compared to the locked FIS in isolation and absorption, respectively. From Fig. 17, the FIS always exhibits isolation behavior before impact (gray). However, a large increase in acceleration can be seen when the FIS experiences impact (black). After this initial increase, the normalized acceleration

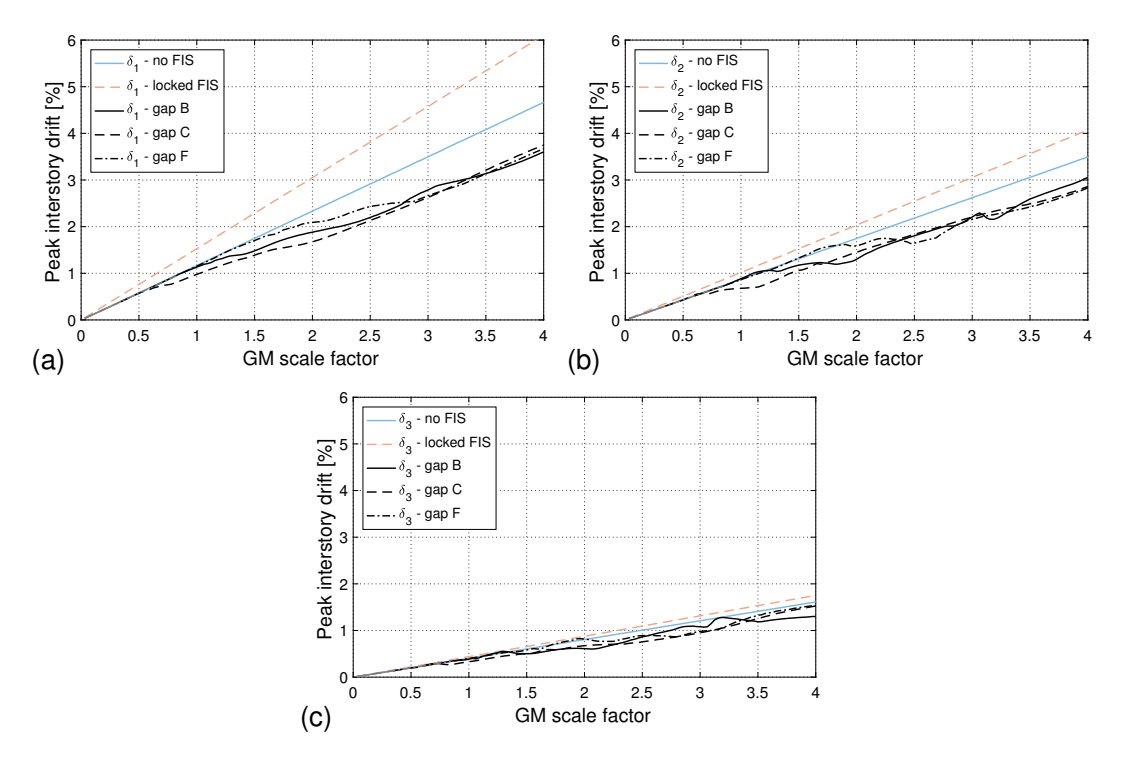


Figure 15: Numerical peak PS responses with different FIS gaps for El Centro: (a) 1st interstory drift  $\delta_1$ , (b) 2nd interstory drift  $\delta_2$ , and (c) 3rd interstory drift  $\delta_3$ . The gray portion indicates cases in which there are no impact whereas the black portion indicates cases in which impacts occurred in the FIS.

fluctuates with an overall decreasing trend as the GM scale factor increases. From Fig. 18, absorption performance can be observed for El Centro, Hachinohe and Northridge, whereas Kobe exhibits poor absorption performance both before and after impact. With respect to the locked FIS, El Centro and Hachinohe exhibit interstory drift reduction both before and after impact. However, significant divergence in drift reduction starts to occur after impact. For El Centro (Fig. 18(a)), the reduction plateaus starting at a scale factor of 3 for all FIS gaps. For Hachinohe (Fig. 18(b)), the drift responses continue to decrease until a scale factor of about 2.5 after which a small increase is observed. For Kobe (Fig. 18(c)), impacts reduce the interstory drift but are not effective enough to reduce the PS's responses compared to the case of locked FIS. For Northridge (Fig. 18(d)), impacts improve the FIS's absorption performance only at small intensities. As seen in Fig. 18(d), from a scale factor of 1 to 4, impacts have no effect on the absorption performance index.

In Figs. 17 and 18, the overall features of the cases with FIS gaps resemble those seen in the experimental results (Figs. 10 and 11, respectively). In all cases, excellent isolation performance ( $J_a \ll 1$ ) can be observed prior to impact, and after impact, there is a drastic increase in FIS acceleration resulting in a degraded isolation performance ( $J_a \gg 1$ ). A direct comparison of the absorption performance index  $J_\delta$  is difficult due to the aforementioned discrepancy in the normalizing case (locked FIS), resulting in a shift in the index  $J_\delta$  for the no FIS and gap cases. Because the gap cases tend toward the no FIS case prior to impact, an alternative metric is used here to facilitate a more direct, quantitative comparison between the numerical and experimental results. Fig. 19 shows the ratio of the peak first story drift  $\delta_1^{\text{max}}$  normalized by  $\delta_1^{\text{no FIS}}$ , the peak drift for the case of no FIS. As a result, this metric tends toward unity for small GM scale factors in the absence of impacts. For the case considered (gap B), good agreement is seen between the numerical and experimental values.

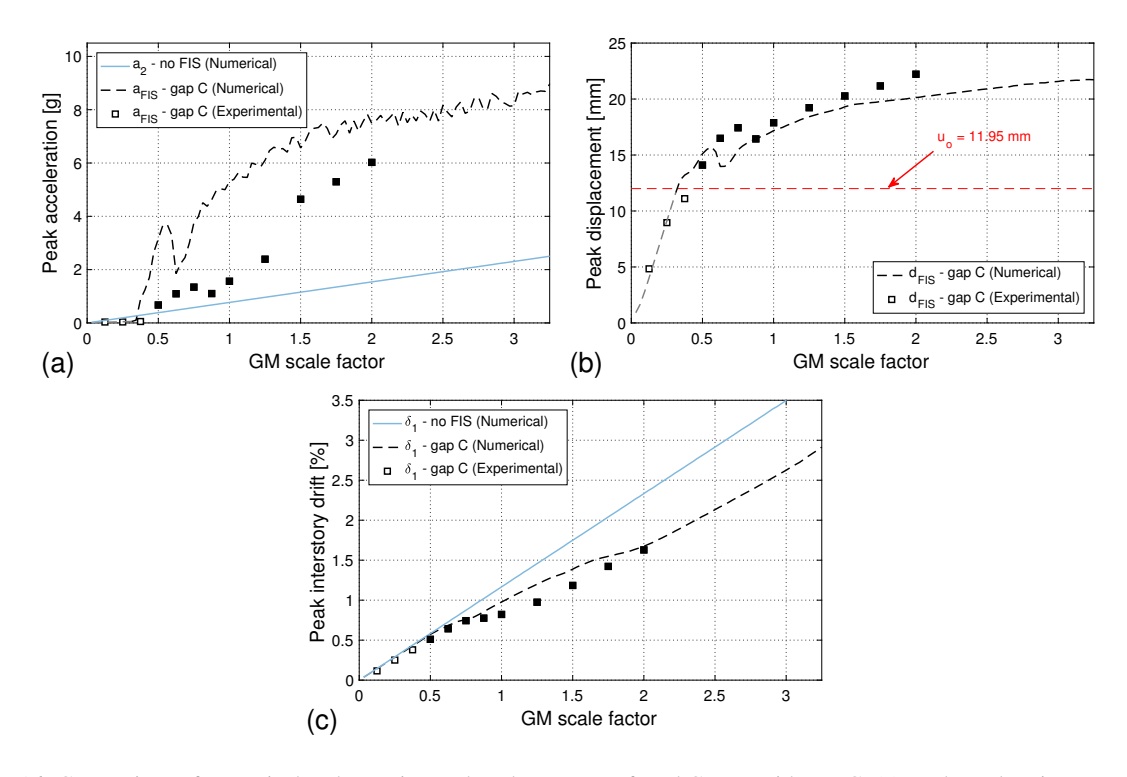


Figure 16: Comparison of numerical and experimental peak responses for El Centro with gap C: (a) total accelerations  $a_2$  and  $a_{FIS}$ , (b) FIS displacement  $d_{FIS}$ , and (c) 1st story drift  $\delta_1$ . The no FIS case is shown for reference in (a) and (c), and the horizontal line in (b) represents the FIS gap  $u_o = 11.95$  mm. The gray lines indicate numerical results in which impacts do not occurr, and the filled markers indicate experimental tests in which impacts occurred.

## 6. Conclusions

This paper evaluated a FIS's isolation and absorption performance by analyzing both analytical and experimental results. A mathematical model of the coupled PS-FIS system was derived for the case of a pendulum-type isolation bearing using Lagrange's equation to enforce the kinematics of rolling/sliding. Experimentally, a rolling-type FIS with a constant radius of curvature track was mounted onto the second floor of a three-story, lab-scale steel structure subjected to four historic ground motions—El Centro, Hachinohe, Kobe, and Northridge. Three FIS gaps—21.95, 11.95, and 32.79 mm—were investigated at varying GM intensity scale factor, which were then compared to baseline cases (i.e., locked FIS and no FIS) in order to evaluate the effectiveness of the FIS as both an isolator and an absorber. The evaluation was conducted using a performance index where the FIS responses are normalized with the responses of locked FIS. The experimental and numerical results showed good agreement, exhibiting similar response-based adaptive performance. Based on the results from these two approaches, it can be concluded that the FIS is capable of protecting sensitive equipment when it displaces within its allowable capacity. Beyond this limit, a reduction in the primary structure's interstory drift can also be observed in some cases, which results in an FIS that is a *dual-mode vibration isolator/absorber system*.

From the experimental and numerical results, the following conclusions can be made: (1) the impact-induced nonlinearity creates a dynamic couple between the FIS and the PS as indicated by the divergence from linear responses, (2) installing a FIS to the PS floor can effectively mitigate seismic response in the isolated content as long as the FIS displacement stays within a linear range, (3) impacts can be harnessed to protect the PS for Hachinohe and El Centro but general ineffective for Kobe and Northridge, (4) while larger

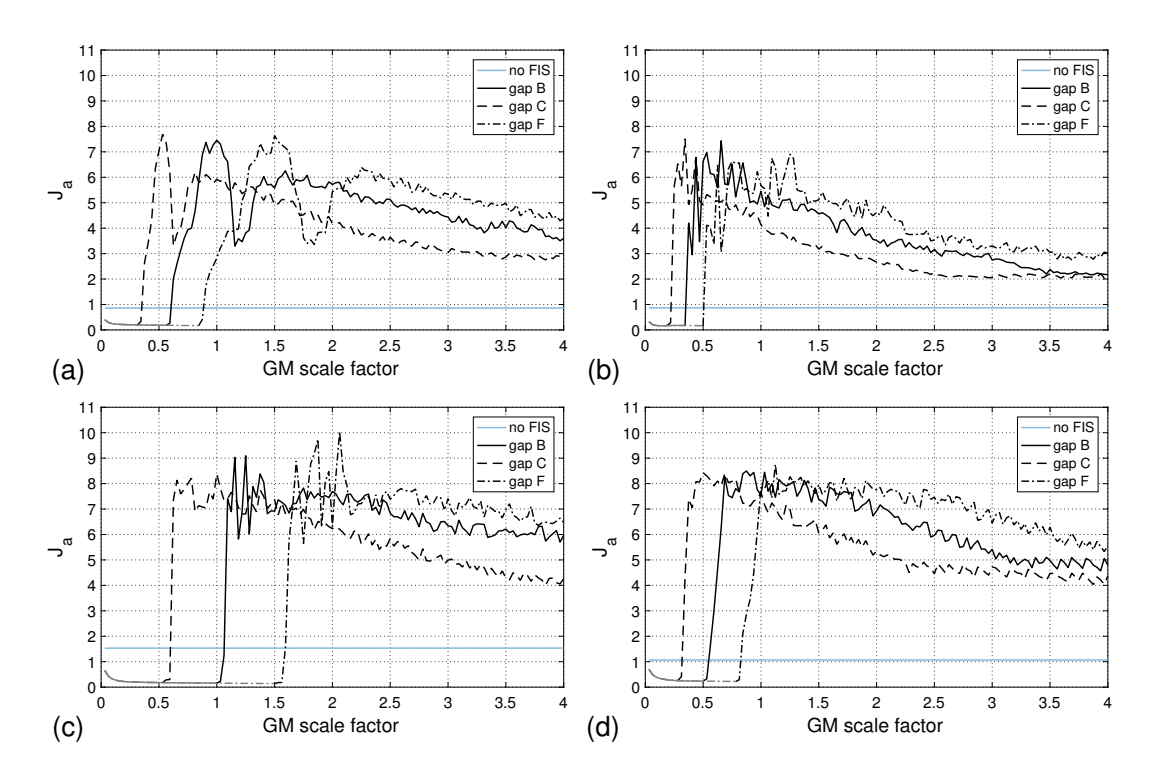


Figure 17: Numerical peak total acceleration performance index  $J_a$  for (a) El Centro, (b) Hachinohe, (c) Kobe, and (d) Northridge. The gray portion indicates cases in which there are no impact whereas the black portion indicates cases in which impacts occurred in the FIS.

FIS gap can isolate more effectively (i.e., at higher intensity scale factors), it does not necessarily provide better absorption performance, (5) smaller FIS gap generally exhibits earlier divergence from the linear response in the absorption performance, (6) higher strong motion duration results in greater absorption performance, and (7) energy redistribution to higher mode in the PS is advantageous to reducing the PS responses.

The results obtained from this research have paved the way for a promising dual-mode seismic isolation system. Future works should take the following extensions into consideration: (1) FIS responses at other stories (i.e., first and third floors); (2) different curving track profiles h(u); (3) various isolation mass ratios; (4) different impact parameters (i.e., shock absorbers with different characteristics); (6) numerical optimization study of the FIS gap that leads to validation testings; (7) consideration of other GMs, focusing on how their frequency content influences the results.

# Acknowledgments

This material is based upon work supported by the National Science Foundation under Grant Nos. CMMI-1663376, OIA-1929151, and CMMI-1943917. This support is greatly appreciated.

#### References

- [1] G. P. Warn, K. L. Ryan, A review of seismic isolation for buildings: Historical development and research needs, Buildings 2 (2012) 300–325, 10.3390/buildings2030300.
- [2] D. Konstantinidis, F. Nikfar, Seismic response of sliding equipment and contents in base-isolated buildings subjected to broadband ground motions, Earthquake Engineering and Structural Dynamics 44 (6) (2015) 865–887, 10.1002/eqe.2490.

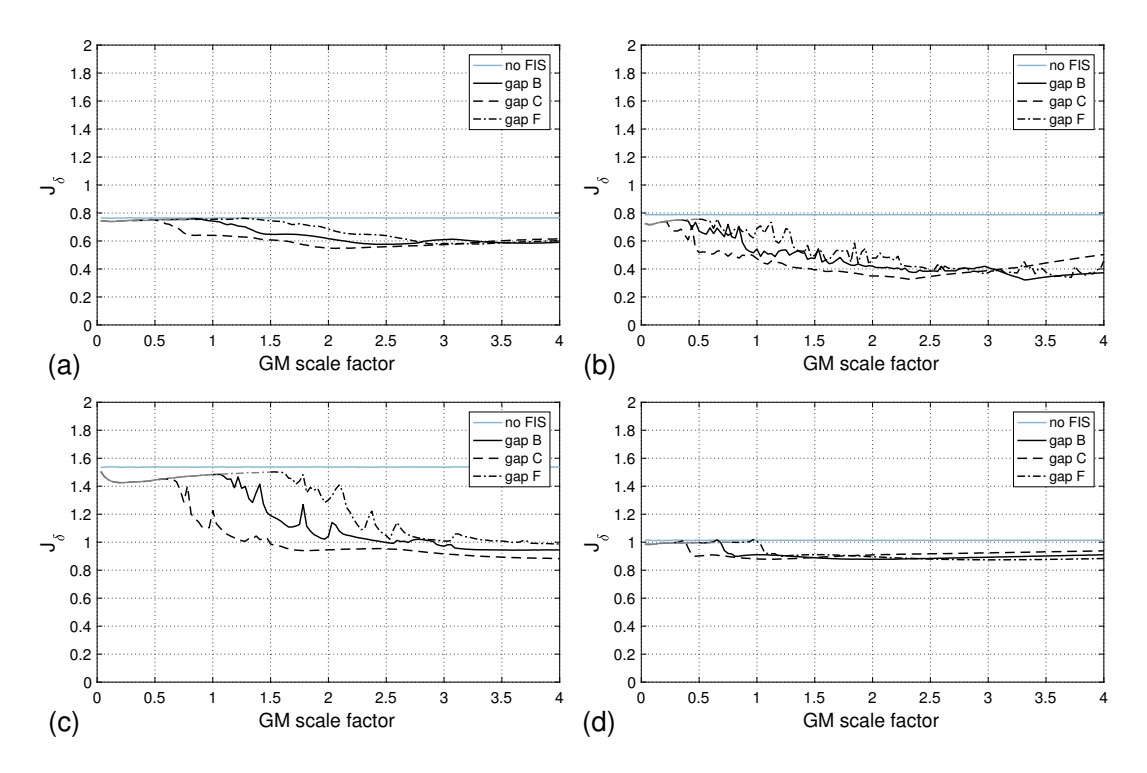


Figure 18: Numerical peak interstory drift performance index  $J_{\delta}$  for (a) El Centro, (b) Hachinohe, (c) Kobe, and (d) Northridge. The gray portion indicates cases in which there are no impact whereas the black portion indicates cases in which impacts occurred in the FIS.

- [3] Y. Shi, M. Kurata, M. Nakashima, Disorder and damage of base-isolated medical facilities when subjected to near-fault and long-period ground motions. Earthquake Engineering and Structural Dynamics 43 (11) (2014) 1683–1701, 10.1002/ege.2417.
- [4] M. C. Chen, E. Pantoli, X. Wang, R. Astroza, H. Ebrahimian, T. C. Hutchinson, J. P. Conte, J. I. Restrepo, C. Marin, K. D. Walsh, R. E. Bachman, M. S. Hoehler, R. Englekirk, M. Faghihi, Full-scale structural and nonstructural building system performance during earthquakes: Part I–Specimen description, test protocol, and structural response, Earthquake Spectra 32 (2) (2016) 737–770, 10.1193/012414EQS016M.
- [5] K. L. Ryan, S. Soroushian, E. Maragakis, E. Sato, T. Sasaki, T. Okazaki, Seismic simulation of an integrated ceiling-partition wall-piping system at E-Defense. I: Three-dimensional structural response and base isolation, Journal of Structural Engineering 142 (2) (2016) 04015130, 10.1061/(ASCE)ST.1943-541X.0001384.
- [6] S. Baggio, L. Berto, T. Favaretto, A. Saetta, R. Vitaliani, Seismic isolation technique of marble sculptures at the Accademia Gallery in Florence: numerical calibration and simulation modelling, Bulletin of Earthquake Engineering 13 (9) (2015) 2719–2744, 10.1007/s10518-015-9741-2.
- [7] C. S. Tsai, Y.-C. Lin, W.-S. Chen, H. C. Su, Tri-directional shaking table tests of vibration sensitive equipment with static dynamics interchangeable-ball pendulum system, Earthquake Engineering and Engineering Vibration 9 (2010) 103–112, 10.1007/s11803-010-9009-4.
- [8] P. S. Harvey, Jr., G.-P. Zéhil, H. P. Gavin, Experimental validation of simplified models for rolling isolation systems, Earthquake Engineering and Structural Dynamics 43 (2014) 1067–1088, 10.1002/eqe.2387.
- [9] S. J. Calhoun, M. H. Tehrani, P. S. Harvey, Jr, On the performance of double rolling isolation systems, Journal of Sound and Vibration 449 (2019) 330–348, 10.1016/j.jsv.2019.02.030.
- [10] C. D. Casey, P. S. Harvey, Jr, W. Song, Multi-unit rolling isolation system arrays: Analytical model and sensitivity analysis, Engineering Structures 173 (2018) 656–668, 10.1016/j.engstruct.2018.06.118.
- [11] P. S. Harvey, Jr., H. P. Gavin, The nonholonomic and chaotic nature of a rolling isolation system, Journal of Sound and Vibration 332 (2013) 3535–3551, 10.1016/j.jsv.2013.01.036.
- [12] V. Lambrou, M. C. Constantinou, Study of seismic isolation systems for computer floors, Tech. Rep. NCEER-94-0020, National Center for Earthquake Engineering Research, 1994.
- [13] M. Hamidi, M. H. El Naggar, On the performance of SCF in seismic isolation of the interior equipment of buildings, Earth-

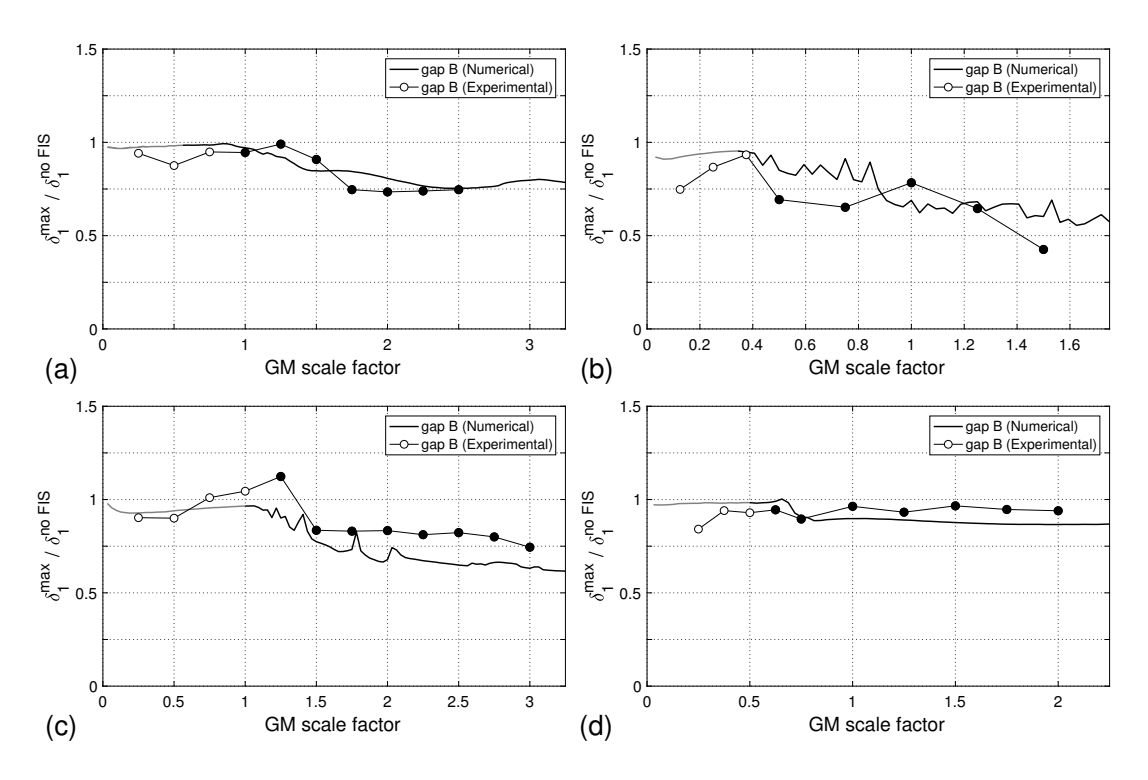


Figure 19: Comparison of numerical and experimental normalized peak 1st interstory drift for (a) El Centro, (b) Hachinohe, (c) Kobe, and (d) Northridge. The gray lines indicate numerical results in which impacts do not occur, and the filled markers indicate experimental tests in which impacts occurred.

quake Engineering and Structural Dynamics 36 (2007) 1581-1604, 10.1002/eqe.708.

- [14] M. Ismail, J. Rodellar, F. Ikhouane, An innovative isolation bearing for motion-sensitive equipment, Journal of Sound and Vibration 326 (2009) 503–521, 10.1016/j.jsv.2009.06.022.
- [15] I. Gidaris, A. A. Taflanidis, D. Lopez-Garcia, G. P. Mavroeidis, Multi-objective risk-informed design of floor isolation systems, Earthquake Engineering and Structural Dynamics 45 (8) (2016) 1293–1313, 10.1002/eqe.2708.
- [16] S. Liu, G. P. Warn, Seismic performance and sensitivity of floor isolation systems in steel plate shear wall structures, Engineering Structures 42 (2012) 115–126, 10.1016/j.engstruct.2012.04.015.
- [17] M. Pranesh, R. Sinha, VFPI: an isolation device for aseismic design, Earthquake Engineering and Structural Dynamics 29 (2000) 603–627, 10.1002/(SICI)1096-9845(200005)29:5(603::AID-EQE927)3.3.CO;2-N.
- [18] R. A. Ibrahim, Recent advances in nonlinear passive vibration isolators, Journal of Sound and Vibration 314 (2008) 371–452, 10.1016/j.jsv.2008.01.014.
- [19] J. P. Den Hartog, Mechanical Vibration, Dover, 1985.
- [20] M. Gutierrez Soto, H. Adeli, Tuned Mass Dampers, Archives of Computational Methods in Engineering 20 (4) (2013) 419–431, 10.1007/s11831-013-9091-7.
- [21] G. W. Housner, L. A. Bergman, T. K. Caughey, A. G. Chassiakos, R. O. Claus, S. F. Masri, R. E. Skelton, T. T. Soong, B. F. Spencer, J. T. P. Yao, Structural control: Past, present, and future, Journal of Engineering Mechanics 123 (1997) 897–971, 10.1061/(ASCE)0733-9399(1997)123:9(897).
- [22] M. M. Murudi, S. M. Mane, Seismic effectiveness of tuned mass damper (TMD) for different ground motion parameters, in: 13th World Conference on Earthquake Engineering, Vancouver, B.C., Canada, paper No. 2325, 2004.
- [23] O. V. Gendelman, T. Sapsis, A. F. Vakakis, L. A. Bergman, Enhanced passive targeted energy transfer in strongly nonlinear mechanical oscillators, Journal of Sound and Vibration 330 (1) (2011) 1–8, ISSN 0022-460X, 10.1016/j.jsv.2010.08.014.
- [24] O. V. Gendelman, Analytic treatment of a system with a vibro-impact nonlinear energy sink, Journal of Sound and Vibration 331 (21) (2012) 4599–4608, 10.1016/j.jsv.2012.05.021.
- [25] J. Wang, N. E. Wierschem, B. F. Spencer, X. Lu, Experimental study of track nonlinear energy sinks for dynamic response reduction, Engineering Structures 94 (2015) 9–15, ISSN 0141-0296, 10.1016/j.engstruct.2015.03.007.
- [26] J. Luo, N. E. Wierschem, S. A. Hubbard, L. A. Fahnestock, D. D. Quinn, D. M. McFarland, B. F. Spencer Jr, A. F. Vakakis,

- L. A. Bergman, Large-scale experimental evaluation and numerical simulation of a system of nonlinear energy sinks for seismic mitigation, Engineering Structures 77 (2014) 34–48, 10.1016/j.engstruct.2014.07.020.
- [27] F. Nucera, A. F. Vakakis, D. M. McFarland, L. A. Bergman, G. Kershen, Targeted energy transfer in vibro-impact oscillator for seismic mitgation, Nonlinear Dynamics 50 (2007) 651–677, 10.1007/s11071-006-9189-7.
- [28] F. Nucera, D. M. McFarland, L. A. Bergman, A. F. Vakakis, Application of broadband nonlinear targeted energy transfers for seismic mitigation of a shear frame: Computational results, Journal of Sound and Vibration 329 (15) (2010) 2973–2994, 10.1016/j.jsv.2010.01.020.
- [29] F. Nucera, F. Lo Iacono, D. M. McFarland, L. A. Bergman, A. F. Vakakis, Application of broadband nonlinear targeted energy transfers for seismic mitigation of a shear frame: Experimental results, Journal of Sound and Vibration 313 (1) (2008) 57–76, 10.1016/j.jsv.2007.11.018.
- [30] J. Wang, N. E. Wierschem, B. F. Spencer, X. Lu, Track Nonlinear Energy Sink for Rapid Response Reduction in Building Structures, Journal of Engineering Mechanics 141 (1) (2015) 04014104, 10.1061/(ASCE)EM.1943-7889.0000824.
- [31] N. E. Wierschem, D. D. Quinn, S. A. Hubbard, M. A. Al-Shudeifat, D. M. McFarland, J. Luo, B. F. Spencer, A. F. Vakakis, L. A. Bergman, Equivalent modal damping, stiffening and energy exchanges in multi-degree-of-freedom systems with strongly nonlinear attachments, Journal of Multi-body Dynamics 226 (2) (2012) 122–146, 10.1177/1464419311432671.
- [32] J. Wang, N. E. Wierschem, B. F. Spencer, X. Lu, Numerical and experimental study of the performance of a single-sided vibro-impact track nonlinear energy sink, Earthquake Engineering and Structural Dynamics 45 (2016) 635–652, 10.1002/ eqe.2677.
- [33] W. Li, N. E. Wierschem, X. Li, T. Yang, On the energy transfer mechanism of the single-sided vibro-impact nonlinear energy sink, Journal of Sound and Vibration 437 (2018) 166–179, 10.1016/j.jsv.2018.08.057.
- [34] P. S. Harvey, Jr., G. Elisha, C. D. Casey, Experimental investigation of an impact-based, dual-mode vibration isolator/absorber system, International Journal of Non-Linear Mechanics 104 (2018) 59–66, 10.1016/j.ijnonlinmec.2018.02.013.
- [35] P. Bin, M. H. Tehrani, M. Nisa, P. S. Harvey, Jr, A. A. Taflanidis, Analysis and optimization of a nonlinear dual-mode floor isolation system subjected to earthquake excitations, Earthquake Engineering and Structural Dynamics 50 (9) (2021) 2334–2354, 10.1002/eqe.3449.
- [36] A. Reggio, M. De Angelis, Combined primary-secondary system approach to the design of an equipment isolation system with High-Damping Rubber Bearings, Journal of Sound and Vibration 333 (9) (2014) 2386–2403, 10.1016/j.jsv.2013.12.006.
- [37] R. Wiebe, P. S. Harvey, Jr, On the Euler-Lagrange equation for systems of rigid-bodies or lumped masses, Journal of Computational and Nonlinear Dynamics 14 (9) (2019) 094502, 10.1115/1.4044145.
- [38] P. S. Harvey, Jr., H. P. Gavin, Truly isotropic biaxial hysteresis with arbitrary knee sharpness, Earthquake Engineering and Structural Dynamics 43 (2014) 2051–2057, 10.1002/eqe.2436.
- [39] L. F. Shampine, M. W. Reichelt, The MATLAB ODE suite, SIAM Journal on Scientific Computing 18 (1) (1997) 1–22, 10.1137/S1064827594276424.
- [40] J. Dorman, P. Prince, A family of embedded Runge-Kutta formulae, Journal of Computational and Applied Mathematics 6 (1980) 19–26, 10.1016/0771-050X(80)90013-3.
- [41] L. Shampine, I. Gladwell, R. Brankin, Reliable Solution of Special Event Location Problems for ODEs, ACM Transactions on Mathematical Software 17 (1991) 1125, 10.1145/103147.103149.
- [42] J. P. Wright, J. Pei, Solving Dynamical Systems Involving Piecewise Restoring Force Using State Event Location, Journal of Engineering Mechanics 138, 10.1061/(ASCE)EM.1943-7889.0000404.
- [43] P. Bin, Evaluating the Performance of a Nonlinear Dual-Mode Vibration Isolator/Absorber System, Master's thesis, University of Oklahoma, Norman, OK, URL https://hdl.handle.net/11244/329571, 2021.
- [44] P. S. Harvey, Jr, P. Bin, Shake Table Tests of a Coupled Primary Structure-Floor Isolation System, in: Experimental Study of the Seismic Performance of a Dual-mode Floor Isolation System, DesignSafe-CI, 10.17603/ds2-r06w-fy29, 2021.
- [45] S. J. Calhoun, P. S. Harvey, Jr., Enhancing the teaching of seismic isolation using additive manufacturing, Engineering Structures 167 (2018) 494–503, 10.1016/j.engstruct.2018.03.084.
- [46] P. S. Harvey, Jr., G. Elisha, Vision-based vibration monitoring using existing cameras installed within a building, Structural Control and Health Monitoring 25 (2018) e2235, 10.1002/stc.2235.
- [47] A. Zare Hosseinzadeh, M. H. Tehrani, P. S. Harvey, Jr, Modal identification of building structures using vision-based measurements from multiple interior surveillance cameras, Engineering Structures 288 (2021) 111517, 10.1016/j.engstruct.2020. 111517.
- [48] Y. Ohtori, R. E. Christenson, B. F. Spencer, Jr., S. J. Dyke, Benchmark Control Problems for Seismically Excited Nonlinear Buildings, Journal of Engineering Mechanics 130 (2004) 366–385, 10.1061/(ASCE)0733-9399(2004)130:4(366).
- [49] R. A. Ibrahim, Vibro-impact dynamics: modeling, mapping and applications, vol. 43, Springer Science & Business Media, 2009.
- [50] O. Makarenkov, J. S. W. Lamb, Dynamics and bifurcations of nonsmooth systems: A survey, Physica D: Nonlinear Phenomena 241 (22) (2012) 1826–1844, 10.1016/j.physd.2012.08.002.

- [51] L. N. Virgin, C. J. Begley, Grazing bifurcations and basins of attraction in an impact-friction oscillator, Physica D 130 (1999) 43–57, 10.1016/S0167-2789(99)00016-0.
- [52] S. W. Shaw, R. H. Rand, The transition to chaos in a simple mechanical system, International Journal of Non-Linear Mechanics 24 (1) (1989) 41–56, 10.1016/0020-7462(89)90010-3.
- [53] P. S. Harvey, Jr., R. Wiebe, H. P. Gavin, On the chaotic response of a nonlinear rolling isolation system, Physica D 256-257 (2013) 36–42, 10.1016/j.physd.2013.04.013.
- [54] M. D. Trifunac, A. G. Brady, A study on the duration of strong earthquake ground motion, Bulletin of the Seismological Society of America 65 (3) (1975) 581–626.
- [55] A. Arias, Measure of Earthquake Intensity, Tech. Rep., Massachusetts Inst. of Tech., Cambridge. Univ. of Chile, Santiago de Chile, 1970.
- [56] N. E. Wierschem, S. A. Hubbard, J. Luo, L. A. Fahnestock, B. F. Spencer, D. M. McFarland, D. D. Quinn, A. F. Vakakis, L. A. Bergman, Response attenuation in a large-scale structure subjected to blast excitation utilizing a system of essentially nonlinear vibration absorbers, Journal of Sound and Vibration 389 (2017) 52–72, 10.1016/j.jsv.2016.11.003.
- [57] M. A. AL-Shudeifat, N. Wierschem, D. D. Quinn, A. F. Vakakis, L. A. Bergman, B. F. Spencer, Numerical and experimental investigation of a highly effective single-sided vibro-impact non-linear energy sink for shock mitigation, International Journal of Non-Linear Mechanics 52 (2013) 96–109, ISSN 0020-7462, 10.1016/j.ijnonlinmec.2013.02.004.
- [58] D. M. Fenz, M. C. Constantinou, Spherical sliding isolation bearings with adaptive behavior: Experimental verification, Earthquake Engineering and Structural Dynamics 37 (2008) 185–205, 10.1002/eqe.750.